Received: 20 May 2020 | Revised: 13 October 2021 | Accepted: 18 January 2022

DOI: 10.1002/stc.2938

RESEARCH ARTICLE

WILEY

An improved ultrasonic computerized tomography (UCT) technique for damage localization based on compressive sampling (CS) theory

Wentao Wang[1,2,3] | **Hui Li**[1,2] | **Chonghe Wang**[1,2] | **Wensong Zhou**[1,2] | **Yuequan Bao**[1,2]

[1]Key Lab of Intelligent Disaster Mitigation of the Ministry of Industry and Information Technology, Harbin Institute of Technology, Harbin, China

[2]Key Lab of Structures Dynamic Behavior and Control, Ministry of Education, Harbin Institute of Technology, Harbin, China

[3]Department of Civil and Environmental Engineering, University of Michigan, Ann Arbor, Michigan, USA

Correspondence
Professor Hui Li, School of Civil Engineering, Harbin Institute of Technology, 202 Haihe Road, Nangang District, Harbin 150090, China.
Email: lihui@hit.edu.cn

Funding information
China Academy of Railway Sciences, Grant/Award Number: 2013G004-A-1; Natural Science Foundation of China, Grant/Award Number: 51378154

Summary

The traditional ultrasonic computerized tomography (UCT) method needs numerous measurements to detect the inside conditions of concrete. Considering the damage is sparsely distributed in the reinforced concrete, compressive sampling (CS) is applied to advance the UCT method at both the measurement stage and the imaging stage to localize damage part in the structure. The proposed detection algorithm requires much fewer measurements compared to the traditional UCT with the same accuracy. In the measurement stage, the pitch–catch paths are randomly selected to capture the travel time of ultrasonic wave from one side to the other side in the dense measurement net. When ultrasonic waves propagate in the structure, they will interact with the damaged part, prolong the propagation length, and delay the time of flight (ToF). In the imaging stage, the whole specimen is divided into small pixels based on the desired accuracy. The conventional Rando equation is advanced based on $\ell 1$-minimization algorithm from CS method to solve the slowness of each pixel to reconstruct the damaged part. The functionality of the proposed algorithm is validated via both numerical model and experimental testing on a reinforced concrete beam in the laboratory. The results reveal the UCT based on CS is more efficient for localizing and imaging the damage with much fewer measurements, which has the immense potential in the development of structural health monitoring (SHM).

KEYWORDS

compressive sampling, computerized tomography, damage identification, nondestructive testing, structural health monitoring, ultrasonic wave

1 | INTRODUCTION

Structural health monitoring (SHM) is an essential management tool that provides quantitative data to evaluate the structural health. SHM consists of global approaches and local nondestructive testing-based (NDT-based) technique to identify damage existence, location, type, and severity for the decision making of maintenance to ensure structural safety.[1–4] Compared to the global approach, NDT-based local damage detection technique which is more sensitive to

the small level of damage provides a more precise interrogation of structural component with a more direct measurement of spatially depicting structural damage.[3,5–7] While local damage detection technique has its own drawbacks such as point-based (strain gauge, thermal sensor) approach, it can only get sensitive damaged response in locations close to the damage. Thus, high-dimension local sensing approaches are pursued to visualize the spatial interrogation of the structure via a network of single point sensor,[8,9] wave-based (e.g., electromagnetic wave and elastic wave) scanning,[5,8,10–12] computerized tomography (CT),[13,14] computer vision,[15,16] etc.

CT technique is a powerful approach to derive high-dimension visualization of the object. While X-ray CT scanning is currently used as a clinical evaluation method, it also exposes human body under the harmful radiation. Thus, for the high-intensity industrial SHM, ultrasonic CT (UCT) become a better approach to interrogate the internal flaw in structures for the characterization of the damages. UCT has been extensively used as 2-D/3-D sensing technique in many areas, such as medical science,[17–21] civil engineering,[22–24] and material engineering.[25] Wiegand and Hoyle used pulse-echo ultrasound tomography to generate a cross-sectional image of the two-phase flow in real time.[26] They do significantly improved signal-to-noise ratio (SNR) and reconstructed image, but the flow imaging can only use a restricted number of sensor positions in their system. Transmission-mode UCT was employed by Xu et al. to analyze the inherent dependency of the incomplete tomographic projections on the distribution of bubbles in gas/liquid flow.[27] The authors pointed out that the accuracy can be furthered by increasing the quantity of transducer, but they also stated that compromise must be made between the increasing resolution and the ability of the system. Ohkawa et al. described the distributions of gas and solid holdups in slurry bubble column by UCT technique.[24] These research showed UCT technique has good reconstruction result in terms of the recognizing the gas–solid systems. Later researches all confirm that UCT is a technique with great significance can be applied to varieties of ranges. In Fujii and Zhang's study, UCT can also be used for temperature measurements.[25] Zhu et al. have presented an UCT algorithm to obtain three-dimensional temperature or CO_2 concentration distributions for environmental field where ultrasonic phase difference were served as projected data.[28] He found out that reconstruction quality can be improved due to the increase of projection data by decreasing the step rotation angle; however, this kind of means may increase the number of measurements. Hay et al. demonstrated that UCT technology is capable of detecting material loss on real aircraft components using embedded piezoelectric sensors on hidden surfaces. Their study showed clearly that the method is very sensitive to material loss[29] demonstrating UCT is a good method for damage detection, but he has the same problem with time consuming related to testing time. Hoyle then reviewed the ultrasound transducers employed in tomography, including their advantages and difficulties.[30] He stated that the use of CT especially fits the condition where significant changes in density or elasticity occurs but the quantity of data also caused problem cannot be solved. Rahiman et al. described the design and modeling of ultrasonic tomography for two-component high-acoustic impedance mixture.[31] Filipik et al. proposed a novel method for calibration of measuring geometry and of individual signal delays of transducers in UCT system.[32] It is worth noting that some researchers applied UCT technique into some civil structures and receive good results. Martin et al. showed that UCT potentially provides a highly successful method of investigating post-tensioned concrete beams.[33] They pointed out that array systems could be developed which would reduce the testing time, the problem is the testing time. Bond et al.[22] applied the UCT method into a dam. They tested the laboratory model and a section of a large dam, but they could not solve the problem between accuracy and resolution for the huge volume of detecting area. These researches all demonstrate that UCT can locate and characterize various structural damages or inhomogeneities of materials.

While the UCT provides a high-dimension visualized damage image, it requires a dense measurement net for detection, which can be costly to provide accurate spatial resolution of the structure. Thus, a cost-efficient reconstruction approach is pursued to shrink the redundant detections from the traditional UCT. Compressive sampling (CS) is a game-changing method to the traditional Nyquist/Shannon sampling theory and has successful achievements since it is proposed by Candès and Wakin,[34,35] Donoho,[36] and Tao et al.[37,38] in 2006. It can accurately reconstruct images or signals to solve ill-conditioned inverse problems from far fewer measurements than are usually considered necessary.[39,40] Nowadays, CS has a significant impact on many applications, such as the signal processing,[38,41] medical imaging[42,43] (especially, the magnetic resonance imaging), geophysical data analysis,[44,45] civil engineering,[46] etc.

In this study, we proposed an efficient method based on CS theory to advance the traditional UCT method to overcome its drawbacks including redundant detection and costly computation. Both the detection stage and imaging stage of the UCT are improved based on CS theory. The entire method will be introduced in the remainder of this paper. First, we introduce the traditional UCT technique and CS theory in Section 2. The cost-efficient UCT method we proposed based on CS theory is also described in Section 2. In Section 3, various simulation models are carried out for random selective inspection to validate the proposed method. The visualized reconstruction results

indicate great agreements with the original damages. In Section 4, we designed and machined a reinforced concrete (RC) specimen with multiple damages for the spatial damage detection. The experimental implement and the reconstruction results are demonstrated in the last part of Section 4. Finally, conclusions and future works are summarized in Section 5.

2 | DAMAGE LOCALIZATION ALGORITHM OF CONCRETE BY IMPLEMENTING CS INTO UCT TECHNOLOGY

2.1 | Brief description of CS approach

The CS approach proposed by Candès[35] can be explained briefly by a mathematic model as following basic example. A common signal $\mathbf{x} \in \Re^N$ can be expended under orthogonal basis which can be expressed in a matrix form as Equation (1).

$$\mathbf{x} = \mathbf{\Psi\alpha}, \tag{1}$$

where $\mathbf{\Psi} \in \Re^{N\times N}$ is the basis matrix, $\boldsymbol{\alpha} \in \Re^N$ is supposed to be K-sparse vector meaning it possesses K nonzero elements ($K << N$).

Original signal then can be compressed by adopting a measurement matrix $\mathbf{\Phi} \in \Re^{m\times N}$ to this procedure can be expressed as Equation (2)

$$\mathbf{y} = \mathbf{\Phi x} + \mathbf{e} = \mathbf{\Phi\Psi\alpha} + \mathbf{e} = \mathbf{\Theta\alpha} + \mathbf{e}, \tag{2}$$

where $\mathbf{\Theta} = \mathbf{\Phi\Psi}$ is an $m \times N$ transfer matrix, the rows of matrix $\mathbf{\Theta}$ are much fewer than the columns, and $\mathbf{e}$ denotes the measurement noises.

The above procedure can be elaborated in a more practical way. Matrix $\mathbf{\Phi}$ can be referred to as m sensors to obtain the partial information of the signal. Therefore, vector, $\mathbf{y}$, with a dimension of m ($m < N$) is the compressive form of signal $\mathbf{x}$ which can be regarded as signal $\mathbf{x}$ received by several arranged sensors.

Construction $\mathbf{x}$ from $\mathbf{y}$ is an underdetermined ill-posed inverse problem because the dimension of $\mathbf{y}$ is much smaller than that of $\mathbf{x}$.[40,47] Fortunately, Candès[35] has proven that $\mathbf{x}$ or $\boldsymbol{\alpha}$ can be uniquely reconstructed with overwhelming probability if the signal $\mathbf{x}$ is sparse and the transfer matrix $\mathbf{\Theta}$ meet the restricted isometry property (RIP). That is, there exists an isometric constant δ_K for the matrix $\mathbf{\Theta}$. Where δ_K is defined as the smallest number which holds for all K-sparse vectors v, such that:

$$1 - \delta_K \le \frac{\|\mathbf{\Theta}v\|_2}{\|v\|_2} \le 1 + \delta_K, \delta_K > 0. \tag{3}$$

This property essentially requires that every set of columns with cardinality less than $\boldsymbol{K}$ are approximately orthonormal. If the columns of the transfer matrix $\mathbf{\Theta}$ are orthogonal, then $\mathbf{x}$ can be exactly constructed from $\mathbf{y}$.[36] Candès also proved that random matrix, such as Gaussian matrix and Bernoulli matrix, could be employed as the measurement matrix to construct the signal. Besides, the measurement number m must be larger than the required number $m > \mu K \log(N/K)$, and μ is a universal constant (independent of K, m, and N).[34,35] This bound is in fact optimal depending on each instance.

If the measurement number is satisfied, one can stably and accurately reconstruct nearly sparse signals from dramatically under-sampled data in an incoherent domain. In the other words, α, the sparse coefficients vector of the original signal x can be exactly or approximately reconstructed from the random low-rate sampling measurement vector y by solving the convex optimization problem.

Foucart and Rauhut[48] proved the "asymptotic" recovery condition for large N, mildly large K, and large ratio N/K, as shown in Equation (4)

$$m > 2K\log(N/K). \tag{4}$$

This is the general rule of thumb for compressive sensing and reflects well empirical tests for sparse recovery using further random matrices such as Gaussian matrices and Bernoulli matrices.

In this study, μ is selected to be 4 to ensure the information can be recovered with high probability. Then, following convex optimization can be employed to obtain $\mathbf{x}$:

$$\text{argmin}\|\boldsymbol{\alpha}\|_1 \text{ subjected to } \|\boldsymbol{\Theta}\boldsymbol{\alpha}-\mathbf{y}\|_2<\varepsilon, \tag{5}$$

where $\|\boldsymbol{\alpha}\|_1=\sum_{i=1}^{N}|\alpha_i|$, and ε is the reconstruction error threshold.

2.2 | UCT technique

UCT technique for damage detection using ultrasonic waves in structures has evolved from the concept of X-ray/UCT used in the medical community.[49] It consists of two stages to obtain the visualized tomographic reconstruction. In the measurement stage, ultrasonic waves are generated with piezoelectric ultrasound probes, transmitted in direction of the structure, and received with another ultrasound probe. While traversing and interacting with the measurement structure, ultrasonic waves carry information of the damage part in the structure,[50–52] e.g., the attenuation, the time of flight (ToF) of the wave, and the scattered wave magnitude as shown in Appendix A. In the imaging stage, the transmission information recorded is extracted and used to create an image of the damage part based on the solution of claassical inverse Radon problem. Considering the ToF from one probe to the other probe as the target function, then, the ToF at the measurement path is equal to the line integral of the travel time of each pixel over the same path.[49,50] Radon provided a basis for the description of the tomographic projections. The ToF along path i can be expressed as follows:

$$T_i=\int_{L_i}\frac{1}{V(x,y)}\mathrm{d}L=\int_{L_i}s(x,y)\mathrm{d}L, \tag{6}$$

where T_i is the travel time along measurement path i, $V(x,y)$ and $s(x,y)$ are the ultrasonic wave velocity and slowness at location (x,y) in the measurement area which are related to the properties of each pixel in the structure, and L_i is the total length of the measurement path i.

Although ultrasonic wave propagation in the structure is 3-D, to simplify the UCT method, the reconstruction processing is demonstrated as a 2-D problem with all the actuators and the sensors placed in the same plane. To reconstruct the damage, the structure is divided into a number of pixels, as shown in Figure 1 (the smaller pixel, the more accurate). The slowness in a grid is considered as a constant in the small pixel. Thus, Equation (6) can be rewritten in discretized representation as follows:

$$T_i=\sum_{j=1}^{w}t_{ij}=\sum_{j=1}^{w}\frac{a_{ij}}{V_j}=\sum_{j=1}^{w}a_{ij}s_j, \tag{7}$$

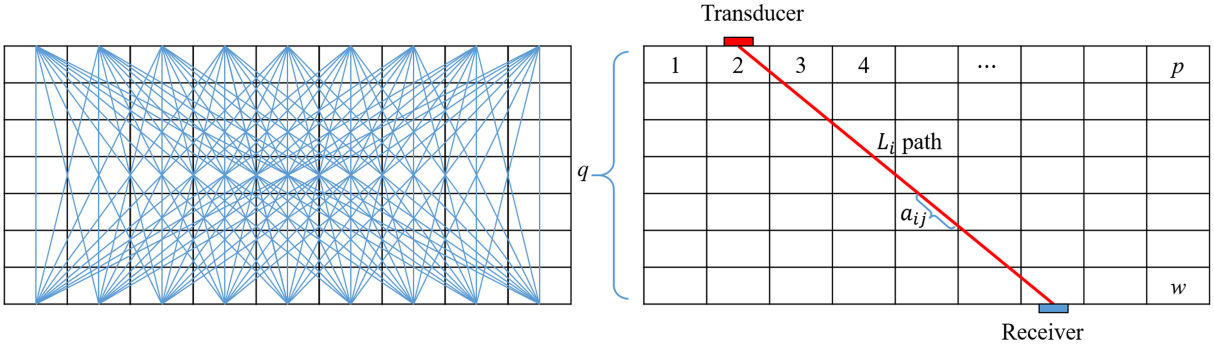

FIGURE 1 UCT technique and the measurement paths

where t_{ij} is the travel time in pixel j along measurement path i, a_{ij} is the travel length of the pixel j in measurement path i, and w is the total number of the pixels, which yields to the product of the number of horizontal and vertical pixels, i.e., $w = p \times q$. For the traditional side-to-side UCT technique, the total number of measurements is $N = p \times p$, where p is the number of the horizontal elements.

Furthermore, Equation (7) can be written in a matrix form

$$\mathbf{T} = \mathbf{AS}, \tag{8}$$

where $\mathbf{T}$ is the vector of travel time of ultrasonic wave along all the measurement paths, $\mathbf{A}$ is the travel length matrix of all the pixels in the measurement paths, and $\mathbf{S}$ is the slowness vector of all pixels.

The overarching goal of imaging stage is to reconstruct the slowness vector $\mathbf{S}$ of the pixels which represents the internal properties and conditions of the structure. There are several algorithms to reconstruct the damage image based on slowness from the measured ToFs, e.g., algebraic reconstruction techniques (ARTs), simultaneous iterative reconstruction techniques (SIRTs), least squares QR (LSQR)factorization, etc. However, as we mentioned previous, the algorithms above require a dense net of paths which contains redundant measurements making the whole processing costly.

2.3 | Damage localization based on CS technology

In order to reduce the measurements of traditional UCT, CS theory is applied to pursue a cost-effective reconstruction via random selective measurement paths. Fortunately, damage (e.g., holes and cracks) distribution is naturally sparse in structures. Therefore, we can regard the slowness of healthy pixels (distributed in most part of the structure) as a reference ($\boldsymbol{S}_0$) to obtain a sparse vector ($\Delta\mathbf{S}$) from the difference between the slowness vector ($\mathbf{S}$) in the measurement structure and reference vector. The sparse slowness vector can be written as

$$\boldsymbol{\Delta S} = \mathbf{S} - \mathbf{S_0}. \tag{9}$$

Combining Equations (9) and (8) yields to

$$\boldsymbol{\Delta T} = \mathbf{T} - \mathbf{T}_0 = \mathbf{A}(\mathbf{S} - \mathbf{S_0}) = \mathbf{A}\Delta\mathbf{S}, \tag{10}$$

where $\Delta\mathbf{T}$ is the difference vector between the ToF of ultrasonic wave propagation in the measurement structure and the reference ToF (healthy structure), and $\mathbf{T_0} = \mathbf{AS}_0$ is the reference ToF vector of the ultrasonic wave in healthy structure. As shown in Equation (9), the ToF difference can be expressed as $\Delta\mathbf{T_0} = \mathbf{A}\Delta\mathbf{S}$, which is directly related to the sparse slowness vector presented above. Equation (10) can be rewritten in the following form:

$$\begin{Bmatrix} \Delta T_1 \\ \Delta T_2 \\ \vdots \\ \Delta T_N \end{Bmatrix} = \begin{Bmatrix} T_1 \\ T_2 \\ \vdots \\ T_N \end{Bmatrix} - \begin{Bmatrix} T_{0\_1} \\ T_{0\_2} \\ \vdots \\ T_{0\_N} \end{Bmatrix} = \begin{bmatrix} a_{11} & a_{12} & \cdots & a_{1w} \\ a_{21} & a_{22} & \cdots & a_{2w} \\ \vdots & \vdots & \ddots & \vdots \\ a_{N1} & a_{N2} & \cdots & a_{Nw} \end{bmatrix} \begin{Bmatrix} \Delta s_1 \\ \Delta s_2 \\ \vdots \\ \Delta s_w \end{Bmatrix}, \tag{11}$$

where ΔT_i is ToF difference obtained from ith measurement path, T_i and T_{0_i} are respectively the measured ToF in the measurement structure with unknow condition and reference ToF along ith path, a_{ij} is the travel length of the jth pixel along ith measurement path, and Δs_j is the slowness of the jth pixel.

Comparing Equation (10) with Equation (1), $\Delta\boldsymbol{T}$ and $\mathbf{A}$ are equivalent to $\mathbf{x}$ and $\boldsymbol{\Psi}$ in Equation (1), respectively. It is worth noted that the travel length matrix $\mathbf{A}$ should be regarded as the dictionary matrix, which is pseudo-random matrix satisfied the RIP condition. Thus, according to previous studies,[36] the unique solution of the convex optimization problem in Equation (5) can be solved in the CS framework.

Then, the CS framework is applied to advance the UCT measurement stage. We randomly select m paths ($m > \mu K \log(N/K)$, $\mu = 4$) from all the N measurement paths to build the measurement net for the ultrasonic inspection of the structure. In mathematics, the m measurement paths selection is expressed as

$$\Delta \mathbf{T}_m^{'} = \mathbf{\Phi}\Delta \mathbf{T}$$
$$\Phi = \begin{bmatrix} 0 & & 1 & & \\ & 1 & & & \\ & & & 1 & \\ 1 & & & & \\ & & & & 1 \end{bmatrix}_{m\times N}, \tag{12}$$

where $\mathbf{\Phi}$ is the measurement matrix representing the selection from the original measurement net of traditional UCT. The matrix is randomly determined by the Bernoulli distribution. In each row of the matrix, one and only one element is equal to 1, and each column will contain at most one element equals to 1. If $\varphi_{ri} = 1$, the ith in all N paths will be selected to interrogate as the rth measurement in the CS-based UCT, and if $\varphi_{rj} = 0$, the jth path will be abandoned for the measurement. In other words, the positions of nonzero element in the measurement matrix $\mathbf{\Phi}$ correspond to the selected measurement paths in the proposed approach.

Substituting Equation (10) into Equation (12), the vector of travel time in the measurement can be rewritten as follows:

$$\Delta \mathbf{T}_m^{'} = \mathbf{\Phi} \cdot \Delta \mathbf{T} = \mathbf{\Phi} \cdot \mathbf{A} \cdot \Delta \mathbf{S} = \mathbf{\Theta}\Delta \mathbf{S}. \tag{13}$$

In order to state the improved UCT in CS framework, Figure 2 is employed to illustrate the proposed method in a flowchart. As shown in Figure 2a, the traditional CT method is summarized to be $\Delta \mathbf{T} = \mathbf{A} \cdot \Delta \mathbf{S}$ as the Radon equation mentioned previously, where $\Delta \mathbf{T}$ is the difference ToF between the measurements from the measured structure and the reference healthy structure, $\mathbf{A}$ is the travel length matrix of all the pixels in the measurement paths, and $\Delta \mathbf{S}$ is the difference slowness vector between the slowness ($\mathbf{S}$) for each pixel and the reference one ($\mathbf{S}_0$) in the healthy structure. It is noted that the slowness vector $\Delta \mathbf{S}$ is a sparse vector with limited number (K) of nonzero entries. Then, for the advanced UCT in the CS framework, a measurement matrix $\mathbf{\Phi}$ is employed to randomly select the measurements from the measurements obtained from the original measurement net. Assuming the number of rows is m ($m > \mu K \log(N/K)$), the measurement matrix $\mathbf{\Phi}$ is sparse and determined by Bernoulli distribution as mentioned in previous. The measurements are assembled to be a new measurement vector, as show in Figure 2a. Meanwhile, the travel length matrix (transfer matrix $\mathbf{A}$) is assembled to be $\mathbf{\Phi A}$ as a result of random selection of measurement paths. $\varphi_{ij} = 1$ means this path is selected and $\varphi_{ij} = 0$ represents the opposite meaning. For example, as Figure 2b,c illustrated, $\varphi_{18} = 1$ states the first ToF difference is obtained from measurement the eighth path of traditional UCT method and the reference ToF. Similarly, $\varphi_{26} = 1$ represents second measurement path of the proposed method is selected to be the sixth measurement path from the original net. Thus, the measurements ToF difference vector ($\Delta \mathbf{T}$) and transfer matrix ($\mathbf{\Theta} = \mathbf{\Phi A}$) are assembled according to the measurement matrix ($\mathbf{\Phi}$) as shown in Figure 2d. It is noted that the measurement paths in the proposed approach are much fewer than that used in the traditional method. As we mentioned previous, the distribution of the damage is sparse ($\Delta \mathbf{S}$ is sparse), and the transfer matrix is a pseudo-random matrix satisfied the RIP condition. Thus, the reconstruction for imaging can be solved by $\ell 1$-minimization algorithm based on CS theory.

$$\Delta \widehat{\mathbf{S}} = \operatorname{argmin}\left(\left\| \mathbf{\Theta} \cdot \Delta \mathbf{S} - \Delta \mathbf{T}_m^{'} \right\|_2 + \lambda \| \Delta \mathbf{S} \|_1 \right), \mathbf{\Theta} = \mathbf{\Phi} \cdot \mathbf{A}, \tag{14}$$

where λ is the Lagrange multiplier in the $\ell 1$-minimization algorithm.

The obtained $\Delta \widehat{\boldsymbol{S}}$ demonstrate both the location and the size of the damage part in the structure. The positions of nonzero element in the vector ($\Delta \widehat{\boldsymbol{S}}$) represent the damage locations, and the value of the nonzero element is related with the severity of the damage in structure. Considering the noise and error in the measurement processing, only the damage value larger than the threshold will be identified as a damage pixel:

$$\left| \Delta \widehat{\mathbf{S}} \right| \geq \Delta \overline{\mathbf{S}}_0, \tag{15}$$

where $\Delta \overline{\boldsymbol{S}}_0$ is the threshold for damage localization.

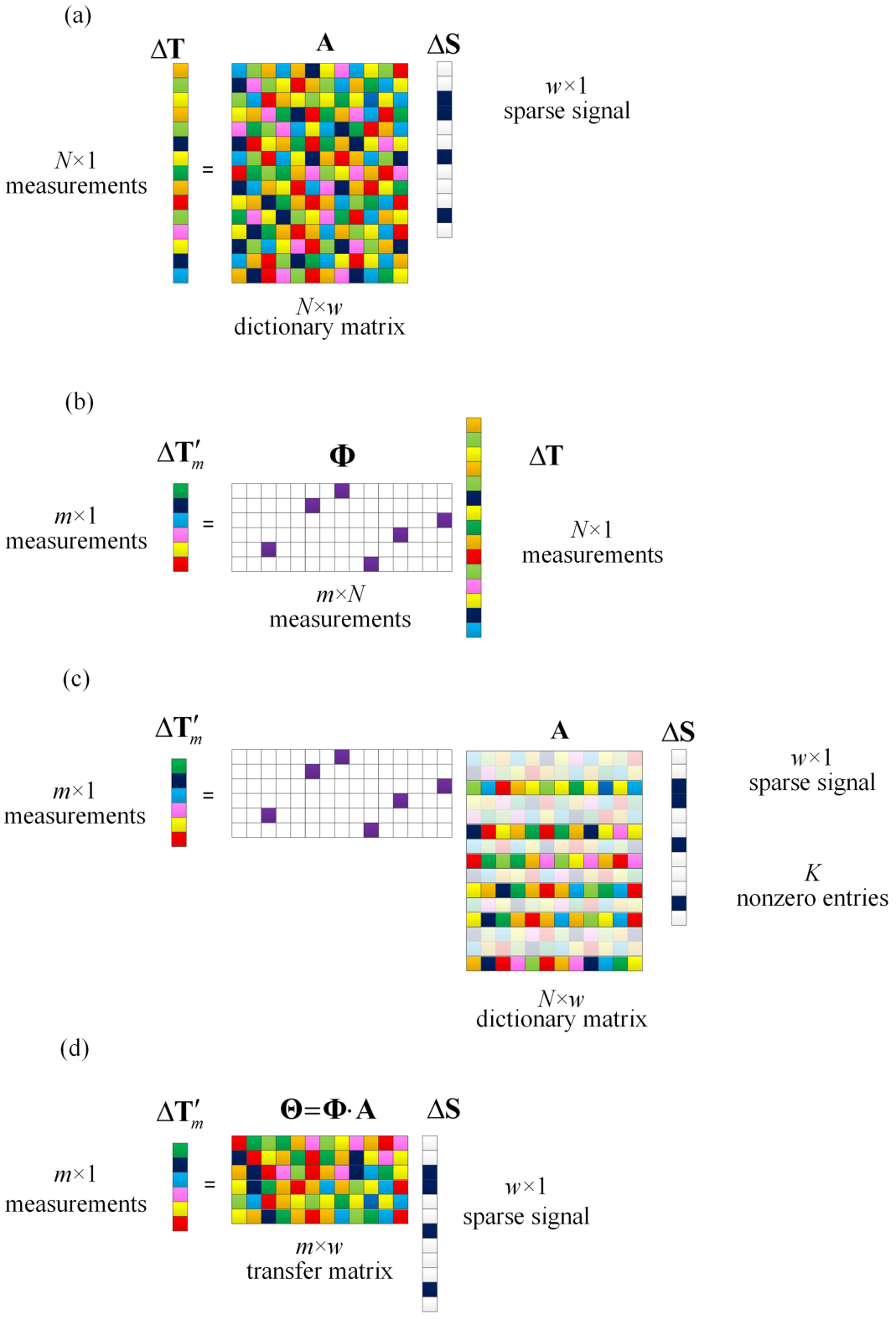

FIGURE 2 Flowchart of the improved UCT technique in CS framework: (a) Radon equation for traditional UCT technique, (b) the proposed approach requires less measurements via a random matrix, (c) improved Radon equation with fewer measurements and random selected paths according to the measurement matrix, and (d) reassembled equation for CS-based UCT approach

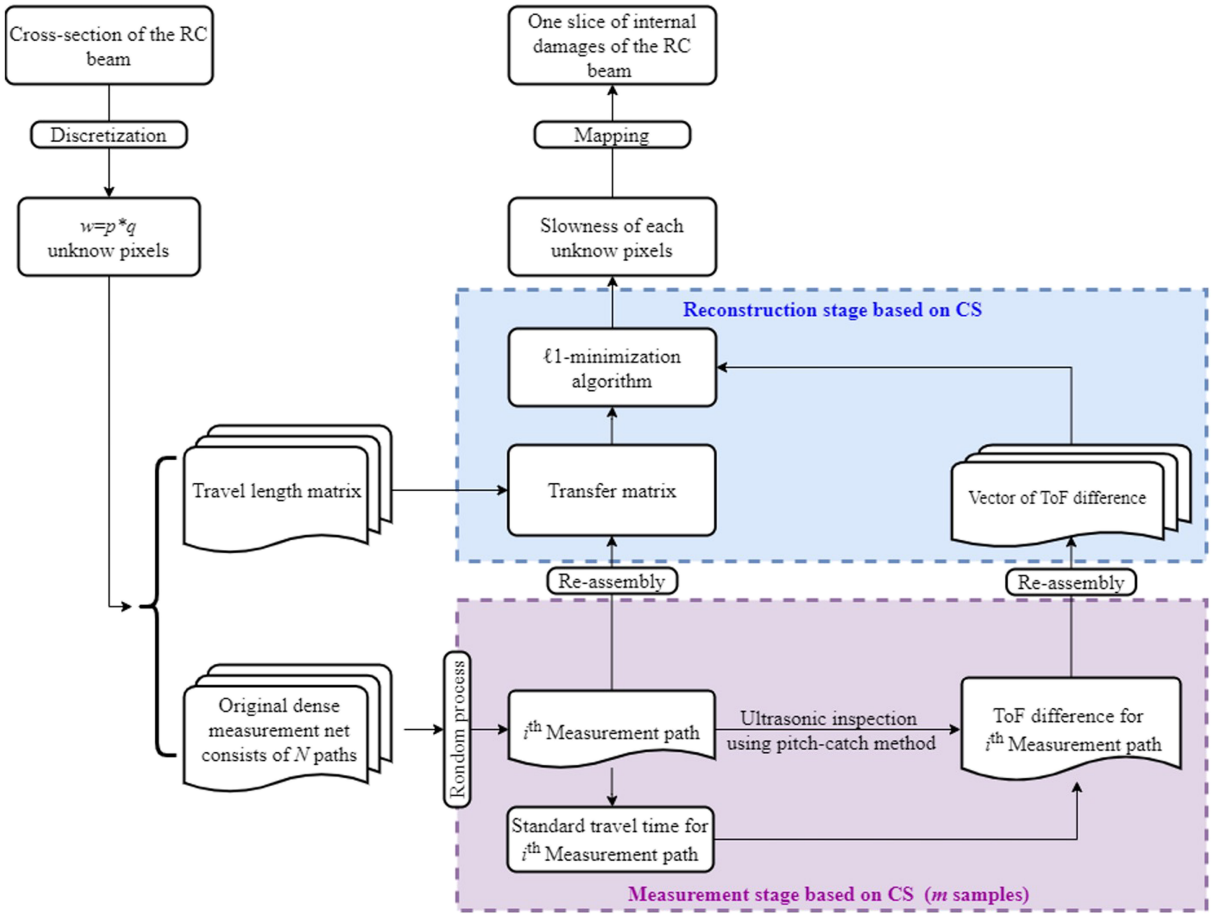

FIGURE 3 Measurement stage and reconstruction stage based on the proposed CS-based UCT technique

In summary, the entire proposed CS-based UCT process can be divided into two stages: measurement stage and reconstruction stage, as shown in Figure 3. As we can see, the discretization process introduces $w = p \times q$ unknown pixels with the given accuracy. Then, the original dense measurement net consisting of N paths and the travel length matrix are determined as well. In the measurement stage, m random processes are employed to choose the measurement paths instead of the even-spaced measurement spots for pitch–catch ultrasonic inspection. The Tof difference for each selected path is calculated based on the standard ToF and re-assembled to a vector of ToF difference feeding to the reconstruction stage. In the reconstruction stage, the reassembled transfer matrix and measured ToF differences are imported into Equation (14) to reconstruct the slowness of each unknown pixel by using the ℓ1-minimization algorithm. Finally, slowness values are mapped to reveal the internal damages as a slice of the cross section of the RC structure.

3 | NUMERICAL STUDY

In order to validate the proposed method, a two-dimension RC beam is modeled for a numerical study. The finite element (FE) modeling platform COMSOL Multiphysics (COMSOL Inc) is adopted to model the RC beam model with various cases of preset damages. The size of the specimen is 1,000 mm (L) × 300 mm (W). Two longitudinal steel bars with diameters of Φ12 and Φ22 are designed, and stirrups are ϕ6@150. The accuracy is respectively selected as 25 and 10 mm along x- and y-axes, in the other words, the pixel size is 25 mm × 10 mm. There are $w = 40 \times 30 = 1{,}200$ pixels in the whole model, as shown in Figure 4. While the traditional UCT method requires 40 excitation points on the top surface and another 40 receiving points on the bottom surface, or vice versa, to solve the inverse problem in Equation (8) for imaging. In summary, $N = 40 \times 40 = 1{,}600$ measuring paths used in traditional UCT to pursue 1,200 unknown values is a huge computational cost. According to that, the size of matrix **A** based on the entire measuring net will also

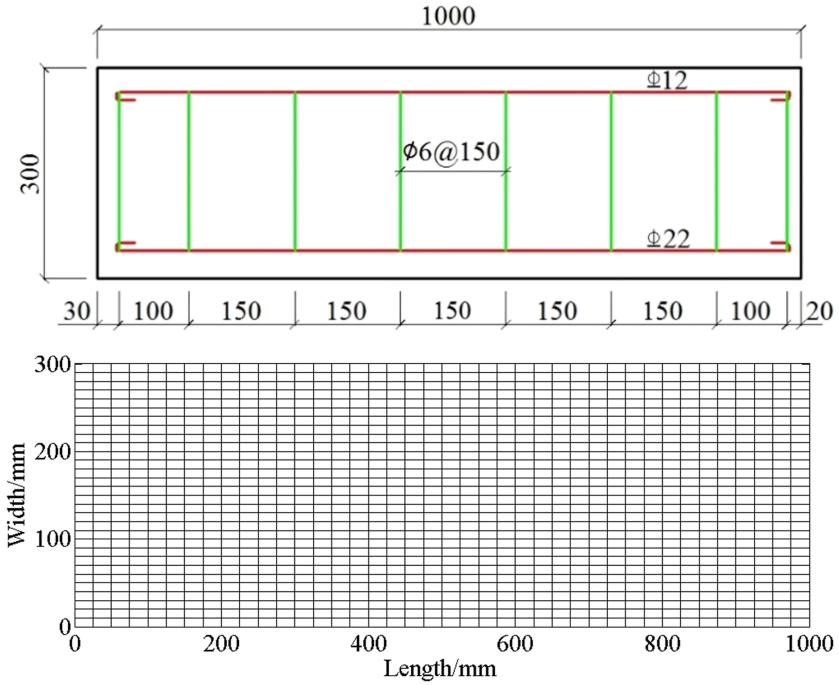

FIGURE 4 RC specimen scheme and 25 mm × 10 mm preset pixels for UCT

be huge and inefficient option for imaging. The entire measuring net consists of 1,600 measuring paths is demonstrated in Figure 5a. As we can see, it is a dense measuring net with significant level of redundancy.

3.1 | Redundancy level of measurement net

As Figure 5b shown, the proposed algorithm randomly selected 200 paths from the original dense 1,600 measurement net for reconstruction. The random selected measuring paths are much sparser than the original net, and the number (measurement workloads) becomes 12.5% of the original 1,600 measurements. The number of measurement paths, $m = 200$, satisfies the requirement that $m > \mu K \log(N/K)$ (in this paper $\mu = 4$), and the transfer matrix satisfies both the RIP and incoherence conditions. The size of measurement matrix $\mathbf{\Phi}$ is 200 (rows) × 1,600 (columns) based on the section above, and the transfer matrix $\mathbf{\Theta} = \mathbf{\Phi A}$ is also reassembled as 200 (rows) × 1,200 (columns) to reconstruct the unknown slowness matrix for imaging. The measurement matrix, $\mathbf{\Phi}$, mapping random selected measurement paths in the original dense net is also shown in Figure 5b.

As shown in Figure 6, the density of path traveling in each pixel of the beam is evaluated to show the redundancy level of the measurement domain. Figure 6a shows the number of measurement paths shared by the same pixel according to the traditional UCT technique. As we can see, the original dense net is high-level redundant for measurement. Although all the pixels in the interested cross section of the beam are covered by multiple measurement paths, it wastes too many measurement paths for evaluating the center of RC beam. A lot of pixels in the center are covered by more than 100 measurement paths each because of the crossing paths. In addition, the distribution of the measurement net is significantly bias distributed. There are more than 100 measurement paths for each pixel in the center; however, only a few paths cover the pixels near the left and right edge of the beam. The maximum and the minimum number of measurement paths shared by one pixel are dramatically different from 115 and 2. The standard deviation and variance are 26.62 and 709.10, which indicate a significantly dispersive distribution of the measurement paths.

The mean value and standard deviation of the number of measurement paths shared by the all the pixels are calculated by Equations (16) and (17)

$$\varepsilon = \frac{1}{w}\sum_{i=1}^{w}\eta_i = \frac{\eta_1 + \eta_2 + \cdots \eta_w}{w}, \tag{16}$$

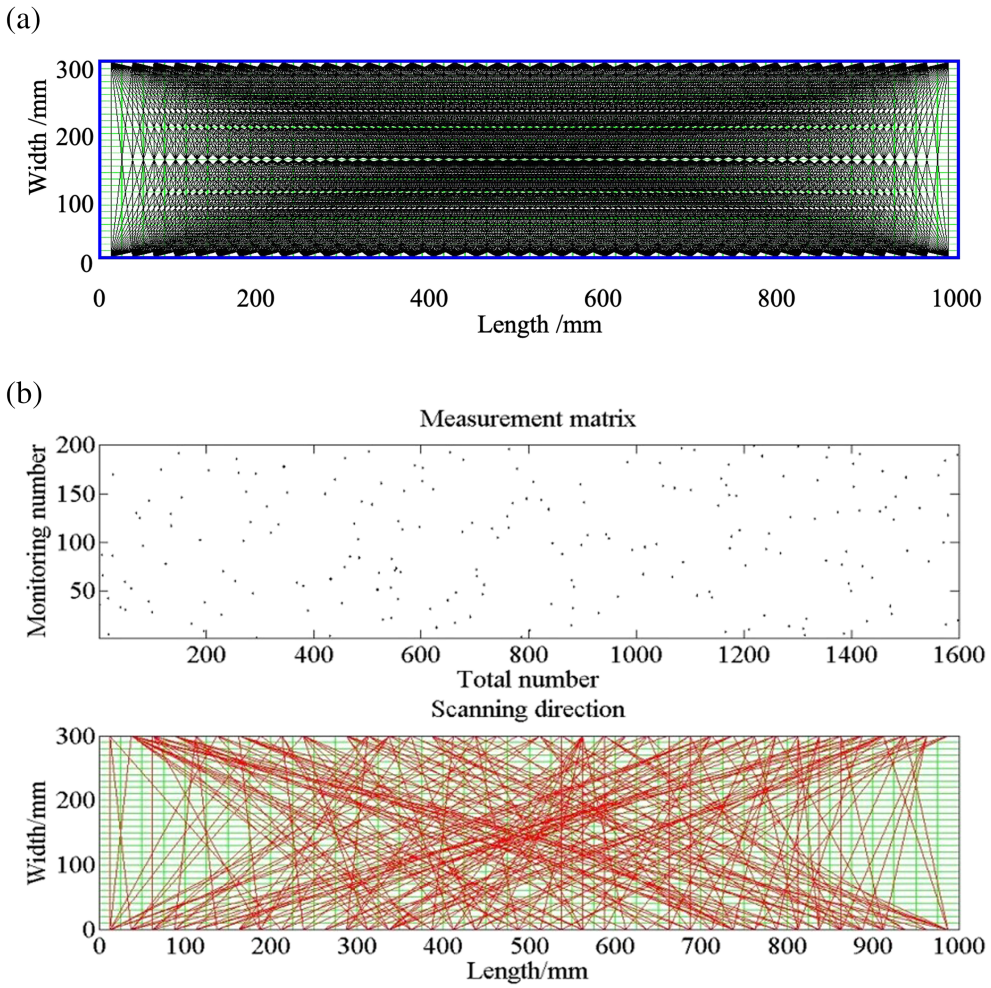

FIGURE 5 (a) Original dense measurement net for traditional UCT; and (b) random measurement matrix and selected measurement paths

$$\sigma = \sqrt{\frac{1}{w}\sum_{i=1}^{w}(\eta_i - \varepsilon)^2}, \tag{17}$$

where η_i is the number of measurement paths covering the ith pixel, ε and σ is respectively the mean value and standard deviation of overlapping paths number for the randomly selected measurement net.

As we can see in Figure 6b, the proposed CS-based UCT introduces a more balanced measurement net. The difference between the central area and edge is much smaller compared to the traditional UCT. The maximum and minimum number of measurement paths shared by one pixel are 19 and 0, respectively. And only 21 pixels on the right edge are not directly measured by this random process. The standard deviation and variance are 3.79 and 14.41, which indicate the 200 measurement paths are well-assigned to evaluate the internal damages of the cross section. In addition, the median value of path number in the same pixel significantly drops from 62.5 to 7.5, which is strong evidence that the proposed method successfully reduces the redundancy level of the traditional UCT.

The distribution of the path number in each pixel for both techniques is demonstrated in Figure 7. For the CS-based UCT, the histogram of measurement net concentrates in the range of 4–10, which means 80% (range of 10%–90%) of the entire 1,200 pixels are covered by 4–10 measurement paths. As comparison, traditional UCT has a slim distribution whose histogram is dispersive from 2 to 115. The path number of the same pixel in the range of 25%–75% is 38–73, and in the range of 10% to 90% is 13–87. The **s**tatistical characters of paths traveling in the same pixel are listed in Table 1 to demonstrate the redundancy level of these two techniques.

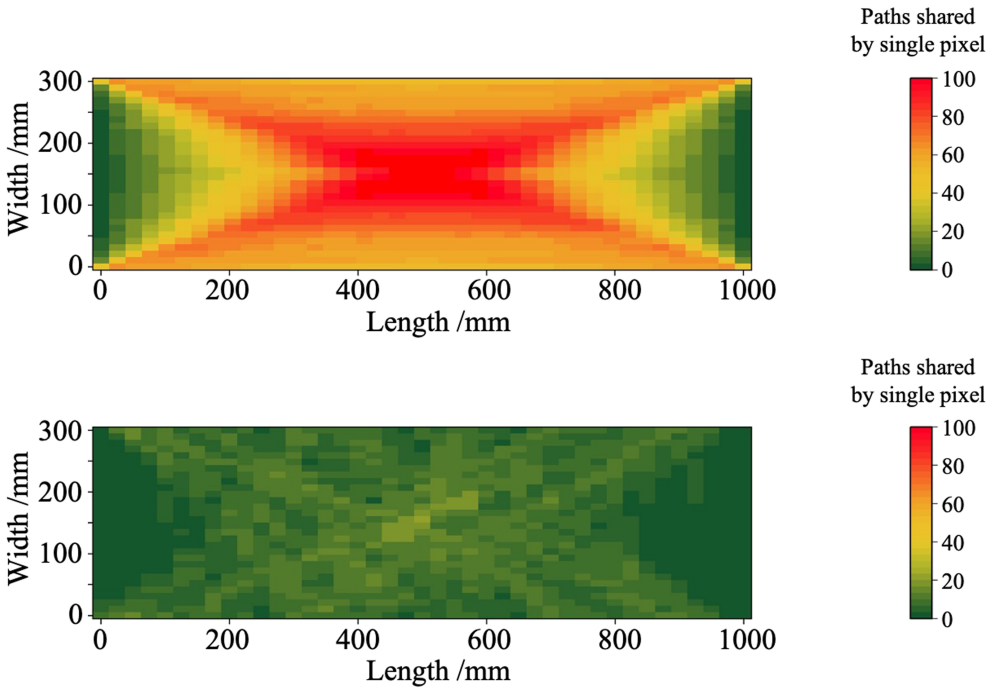

FIGURE 6 The density of paths traveling in each pixel of the beam (a) traditional UCT and (b) proposed CS-based UCT

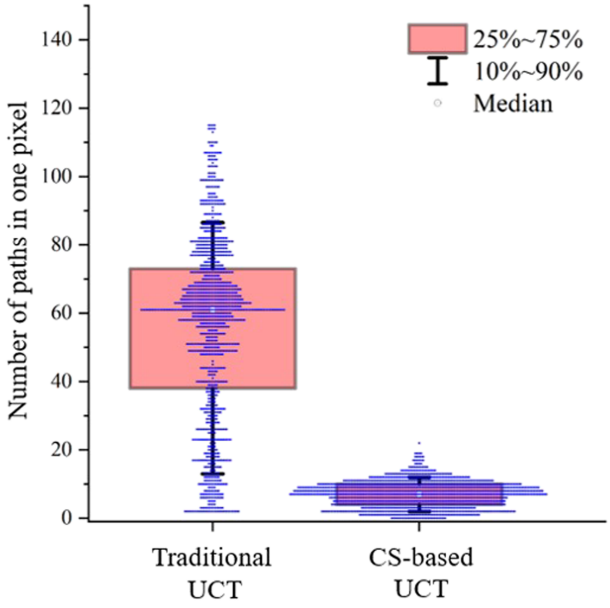

FIGURE 7 Distribution of the path number in each pixel

General speaking, the level of redundancy is witnessed to the change of mean value of overlapping paths number, ε. In addition, a balanced net with well-assigned measurement paths is essential to the CS-based UCT method, because we have to ensure there are as few as possible pixels uncovered. Thus, a novel baseline-free index, β, is defined as

$$\beta = \frac{1}{\varepsilon e^{\sigma}} = \frac{\exp(-\sigma)}{\varepsilon}, \tag{18}$$

where the $\exp(\cdot)$ or $e^{\cdot}$ stands for exponential function, the proposed β index decreases with the increasing of mean value of the overlapping paths number, and it significantly drops when the standard deviation increases. Higher value

TABLE 1 Statistical characters of paths traveling in the same pixel

	Traditional UCT	CS-based UCT
Maximum	115	19
Minimum	2	0
Mean	55.93	7.04
Median	62.5	7.5
Standard deviation	26.62	3.79
Variance	709.10	14.41

of β index represents a better random-selected measurement net for CS-based UCT. Ideally, the proposed index will reach its maximum value, $\beta_{max} = 1$, when the $\varepsilon = 1$ and $\sigma = 0$, which means each pixel is covered by one and only one measurement path.

The β index for the traditional measurement net and aforementioned random selected net is 4.9140e-14 and 0.0032, respectively. Considering the value is extra small, the authors also suggest the natural logarithm function of β index as listed in Equations (19) and (20) to advance our understanding of well-assigned measurement net in the real-world applications.

$$\ln(\beta) = -\ln(\varepsilon e^{\sigma}) = -\ln(\varepsilon) - \sigma. \tag{19}$$

$$\chi = C + \ln(\beta) = C - \ln(\varepsilon) - \sigma, \tag{20}$$

where $\ln(\cdot)$ denotes the natural logarithm function, C is a constant to ensure the positive value of χ index, and χ represents the χ index value of the random-selected measurement net. For instance, $C = 100$, the χ index of the ideal measurement net is $\chi = 100$. The χ index for the traditional measurement net and aforementioned random-selected net becomes 69.36 and 94.26, respectively.

On the contrary, γ index, which is the reciprocal of the index β can be used to present the level of redundancy and chaos degree for the measurement net, as shown in Equation (19).

$$\gamma = \frac{1}{\beta} = \varepsilon e^{\sigma}. \tag{21}$$

3.2 | Numerical model of RC specimen

To verify the proposed method, three cases with various damage types, locations, and numbers are studies on the aforementioned numerical model. Case 1 is the RC specimen without any damage, Case 2 is the RC specimen with five hole-like damages, and Case 3 is the RC specimen with six damages, including two cracks and four holes. The damages in Cases 2 and 3 are randomly generated to prove the functionality of the proposal method, and all these three numerical cases are also adopted to random measurement matrix $\mathbf{\Phi}$ for paths selecting.

As shown in Figure 8a, the concrete beam is isotropic and modeled with mechanical properties as follows: elastic modulus $E_c = 25$ GPa, density $\rho_c = 2{,}400\,\text{kg/m}^3$, and Poisson's ratio $\nu_c = 0.20$. The beam is meshed using 125,553 free tetrahedra (4-node) 3-D elements (Figure 8a). The maximum element size should be less than 1/10th of wavelength of the pressure wave to pursue accurately wave propagation.[12,53] The maximum size for the element is 7 mm, the growth rate is 1.2, and the curvature factor is 0.25 in the user-controlled mesh settings.

The steel-reinforced rebars and stirrups are meshed using a 4-node, free tetrahedra element with a feature size no bigger than 7 mm resulting in a total of 23,947 mesh elements, as shown in Figure 8b. The density of the steel is 7,850 kg/m^3, and the elastic modulus and Poisson's ratio is $E_s = 200$ GPa and $\nu_c = 0.30$, respectively.

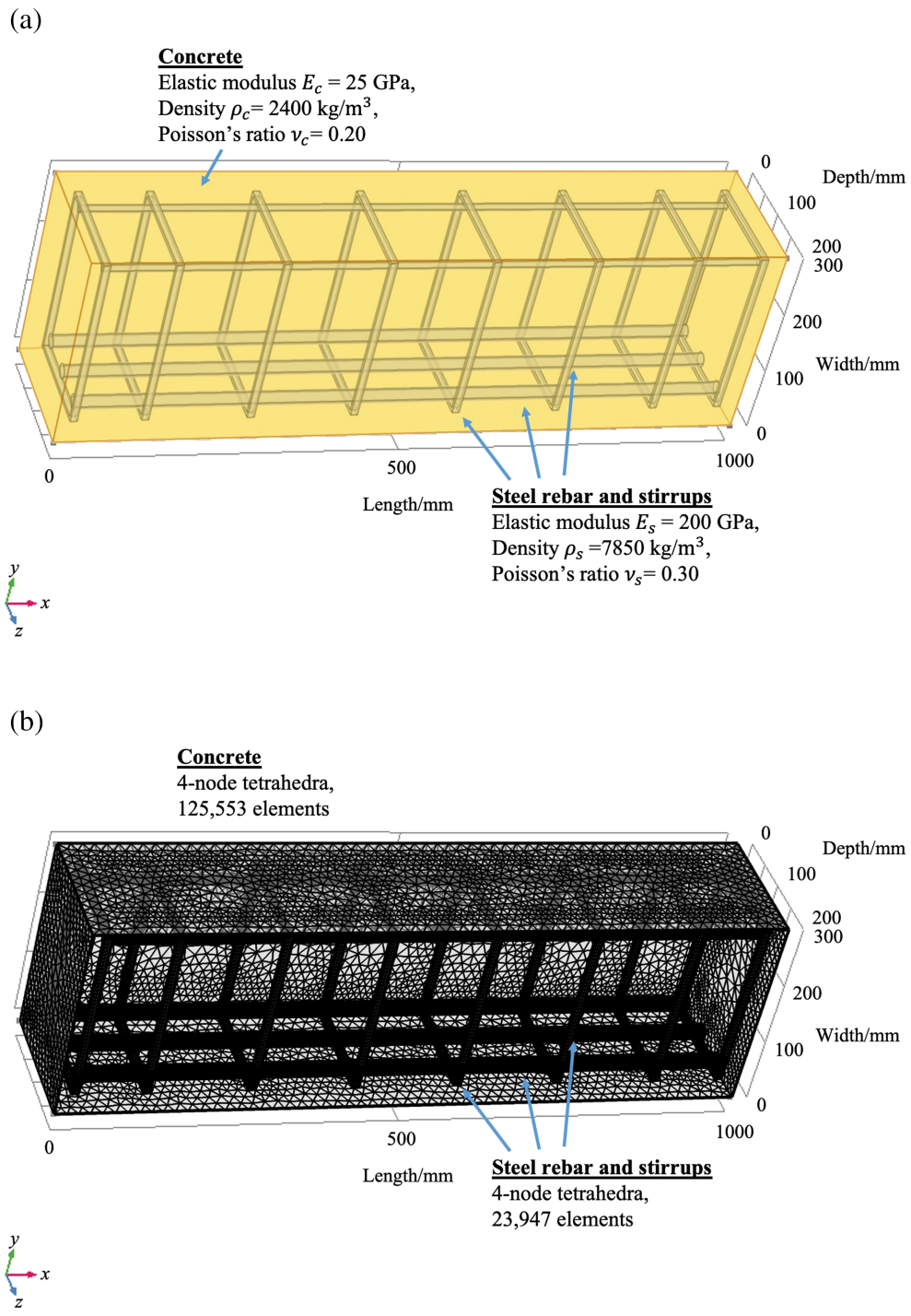

FIGURE 8 (a) Numerical RC model; and (b) meshes for various components

Cracks, holes, and void are created by rectangle or circle partition objects based on Boolean's difference. Thus, the damaged concrete beam in Cases 2 and 3 is regenerated and assembled for numerical simulation, and no extra mesh is needed to mimic the preset damages.

Elastic wave, time explicit (*elte*) module is employed to simulate the time-dependent process of elastic waves propagation in the RC beam specimen. Because of the transmission gel in the real ultrasonic inspection, only pressure wave propagates from the piezoelectric transducer into the RC beam. In general, the pressure wave velocity in concrete and steel are determined by their elastic modules and density,[54–56] as shown in Equations (22) and (23).

$$C_{Pc} = \sqrt{\frac{E_c}{\rho_c}}, \tag{22}$$

$$C_{Ps} = \sqrt{\frac{E_s}{\rho_s}}, \tag{23}$$

where C_{Pc} is the generic velocity of ultrasound propagating in concrete, E_c and ρ_c are the elastic modulus and density for concrete beam, and C_{Ps}, E_s, and ρ_s are the ultrasound velocity, elastic modulus, and density for steel material. In this study, the velocities of pressure wave in concrete and steel are approximately 4,200 and 5,200 m/s, respectively.

After launched by the ultrasonic probe, ultrasonic wave will propagate into the structure, and it will bypass the damage and continue propagating to the probe on the other side. The ToF is obtained by the division of the travel length calculated based on the Huygens–Fresnel principle and the given ultrasonic velocities of concrete and steel.

A capped periodic signal, $V(t)$, is employed as the excitation signal for the piezoelectric transducer, whose formula is as follows:

$$V(t) = \begin{cases} A_c & |v(t)| \geq A_c \\ \mathrm{A}_w \sin(2\pi f_c t) & |v(t)| < A_c \end{cases}, \tag{24}$$

$$v(t) = \mathrm{A}_w \sin(2\pi f_c t), \tag{25}$$

where A_w is the amplitude value of the sinusoid wave, $f_c = 50\,\mathrm{kHz}$ is the center frequency of the excitation signal, t denotes the time, $v(t)$ is the original sinusoid wave, and A_c is the cap of the preset maximum amplitude value of the excitation signal. The amplitude cap, $A_c = 250\,\mathrm{V}$, is utilized to protect the ultrasonic NDT instrument in the following experimental section.

The wavelength of ultrasound when the sinusoidal waveform travels in the concrete or steel rebars at a constant speed C_{Pc} or C_{Ps}, is a given by Equations (26) and (27).

$$\lambda_C = \frac{C_{Pc}}{f_c}, \tag{26}$$

$$\lambda_S = \frac{C_{Ps}}{f_c}, \tag{27}$$

where λ_C and λ_S represent the ultrasonic wavelengths in concrete and steel rebars, respectively.[56] According to the previous research,[12,53] the maximum element size should be less than 1/10th of wavelength of the pressure wave to ensure an accurate wave propagation simulation.

3.2.1 | Case 1

The first case for simulation is the pristine RC specimen which denotes the undamaged (health) status. As shown in Figure 9a, the ultrasounds excited at the location (415 mm, 300 mm) propagate in the model and T_i equals to T_{0_i} in Equation (11) resulting in $\Delta\mathbf{T}$ a zero vector. Thus, the vector of the variation in slowness $\Delta\mathbf{S}$ obtained by the ℓ1-minimization algorithm in Equation (14) is a zero vector as well. The reconstruction result is shown in Figure 9b, and green color denotes the RC specimen is undamaged.

3.2.2 | Case 2

For Case 2, the RC specimen consists of five hole-like damages (holes or voids). Three of them have a diameter of 10 mm located at (200 mm, 150 mm), (300 mm, 200 mm), and (800 mm, 100 mm). Another two 20-mm-diameter holes

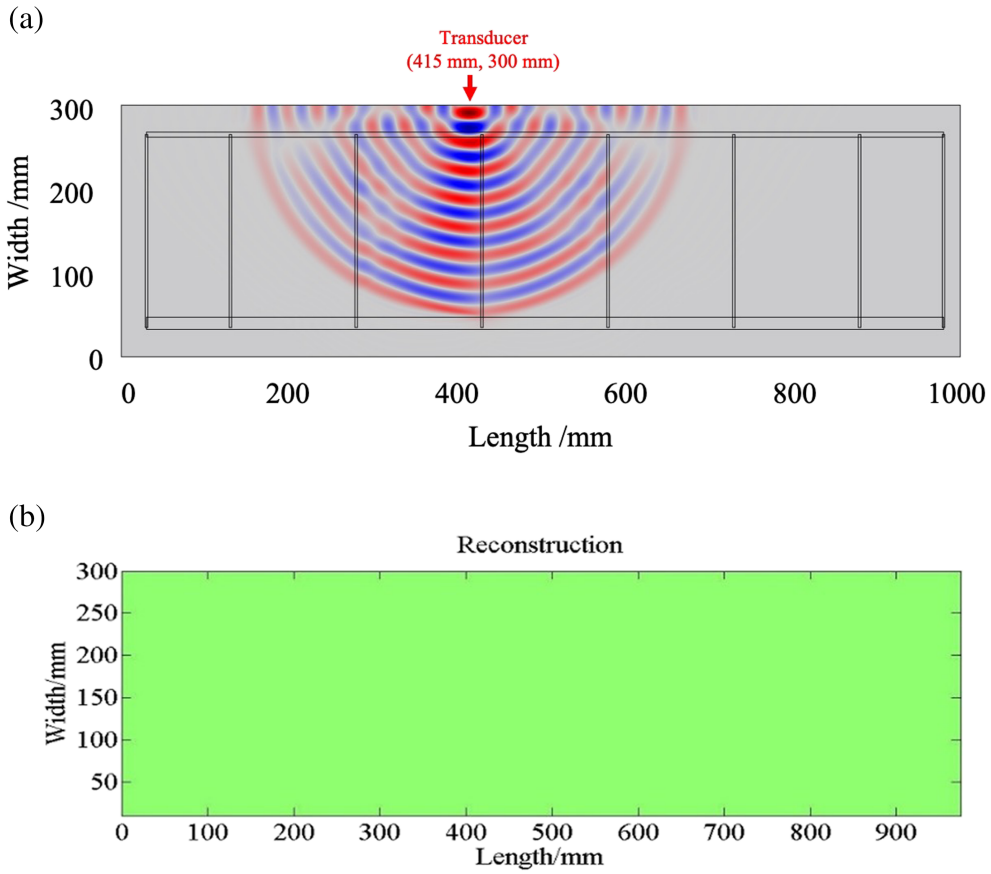

FIGURE 9 (a) Wave propagation example when the transducer locates at (415 mm, 300 mm); and (b) reconstruction results for the undamaged case

(or voids) site at (600 mm, 200 mm) and (400 mm, 100 mm). Two wave propagation examples are shown in Figure 10a when the transducer locates at (415 mm, 300 mm), the receiver at (395 mm, 0 mm), and the transducer locates at (600 mm, 300 mm), the receiver at (300 mm, 0 mm).

Based on Huygens–Fresnel principle, the ultrasonic traveling along the pink line is larger than that without any damage (yellow line). In addition, for various ultrasonic measurement paths, the influence caused by hole-like damages is omnidirectional, which means the pixel containing holes (or voids) has approximately the same effect to the slowness value no matter the direction of the measurement paths. As we can see in Figure 10b, the wavefronts are similar for Paths 1 and 2. The hole respond to ultrasonic waves is used to distinguish from cracks in the RC beam.

The reconstruction results are represented in relative slowness and relative error, as shown in Figure 10c. As we can see, not only the locations but also the relative slowness values of the identified damages have good agreements with the preset damages in Figure 10a. And the small value of reconstruction error is strong evidence that the damages in that cross section have been successfully reconstructed by the proposed method.

3.2.3 | Case 3

In Case 3, four types of damages consisting of throughout holes, blind hole, throughout crack, and half-through crack are designed in the RC model as shown in Figure 11. Two throughout holes whose diameter is 20 mm locating at (200 mm, 200 mm) and (600 mm, 100 mm), another throughout hole whose diameter is 10 mm sitting at (800 mm, 200 mm). A 10-mm-diameter blind hole is located at (400 mm, 100 mm) whose depth diameter is 100 mm starting from the $z = 0$ plane. Meanwhile, a vertical crack whose center is (500 mm, 150 mm) is a throughout crack with a size of 100 mm $\times$ 0.5 mm. And the horizontal crack with the same size is a half-through crack at the location of (650 mm, 200 mm) in the RC model.

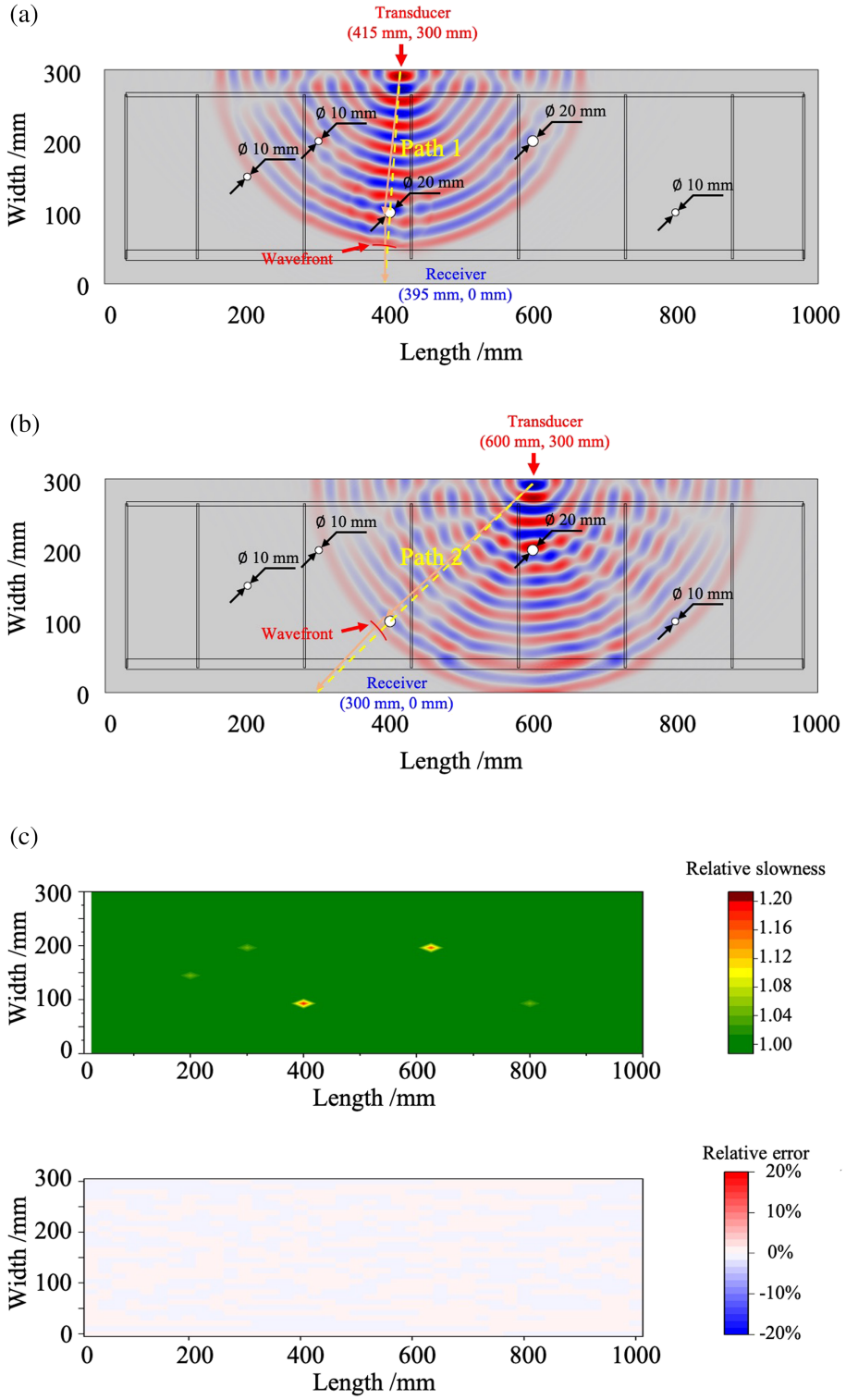

FIGURE 10 Numerical simulation of the RC specimen (Case 2): (a) wave propagation example when the transducer locates at (415 mm, 300 mm) and the receiver at (395 mm, 0 mm), (b) wave propagation example when the transducer locates at (600 mm, 300 mm) and the receiver at (300 mm, 0 mm), and (c) reconstruction results represented in relative slowness and relative error

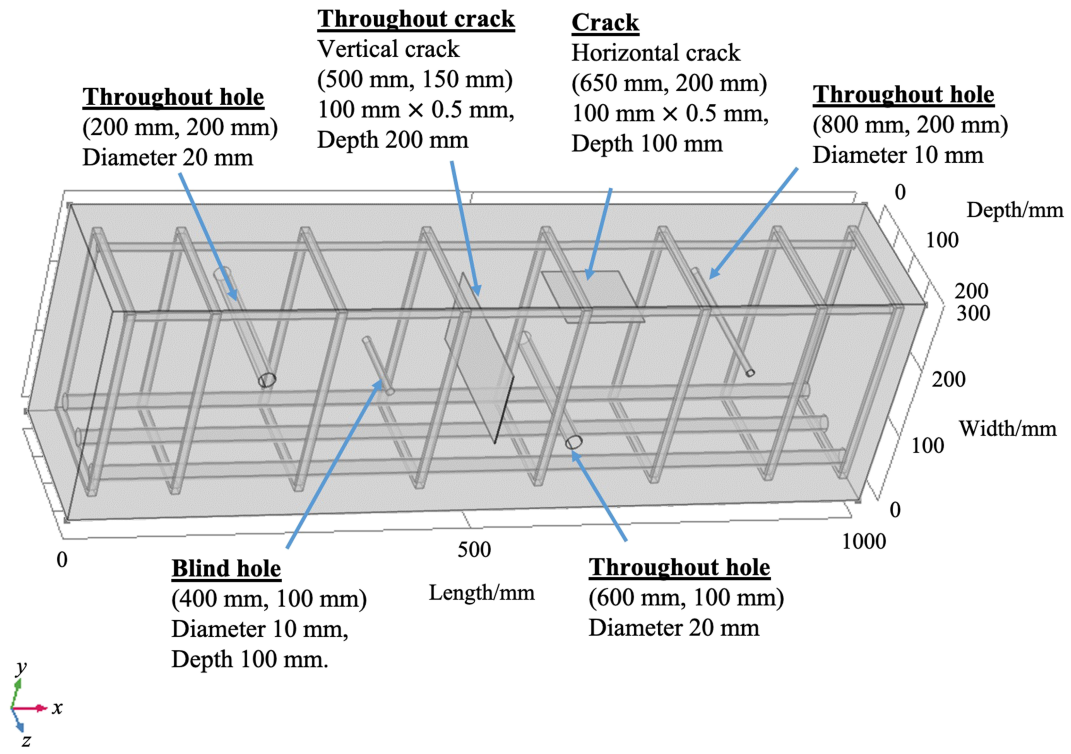

FIGURE 11 Preset damages in the numerical RC model for the Case 3

Similar to the identification of the hole-like damage, the orientation of the crack can be identified by various measurements related to the directional property of crack. For instance, the travel length is 300.10 mm via Path 1 resulting in almost 0 μs of ToF difference, and the travel length for Path 2 is 358.74 mm resulting in approximately 1.5 μs of ToF difference. In addition, the wavefronts are completely different, as we can see in Figure 12b.

Because of the blind hole and normal crack, the proposed methods are utilized twice at $z = 50$ mm and $z = 150$ cross-sectional planes to identify the internal damaged images for demonstration. The slowness values of the pixels on the two planes are separately identified by the $\ell 1$-minimization method. The reconstructed results are shown in Figure 13. Two z-plane slices of the reconstruction results are stacked in Figure 14 to reveal the damage conditions of different depths in the numerical RC model. The identified results of the $z = 50$ mm plane have six damages whose locations have good agreements with the preset damages in the numerical RC model. For the results of $z = 150$ mm plane, four damages are identified because the depths of blind hold and half-through crack are smaller than that of the inspection plane.

4 | EXPERIMENTAL RESULTS AND ANALYSIS

In order to validate the proposed UCT approach in the real world, a RC specimen with a length of 1,000 mm, width of 300 mm and thickness of 200 mm is designed and built with C40 concrete. The reinforced steel bars in the specimen are 2Φ 12 and 3Φ 22, and stirrups are ϕ 6@150, as shown in Figure 15. Four holes and three crack are set by PVC tubes and iron plates to simulate the damage part in the RC specimen. The diameter of holes are 15 (one holes), 10 (one holes), and 20 mm (two holes). Three cracks with the same size of 100 mm × 3 mm were arranged in the angle of 0°, 45°, and 90° respectively.

In the measurement stage, an ultrasonic NDT instrument, NU 62 with two piezoelectric probes, is employed to generate and receive ultrasonic wave on the two sides (top and bottom sides) of the specimen to measure the ToF using pitch–catch method. The actuator probe is attached to the top surface of the specimen to generate continuous square ultrasonic wave with a frequency of 50 kHz and amplitude of 250 V into the RC specimen. The sensor is employed to

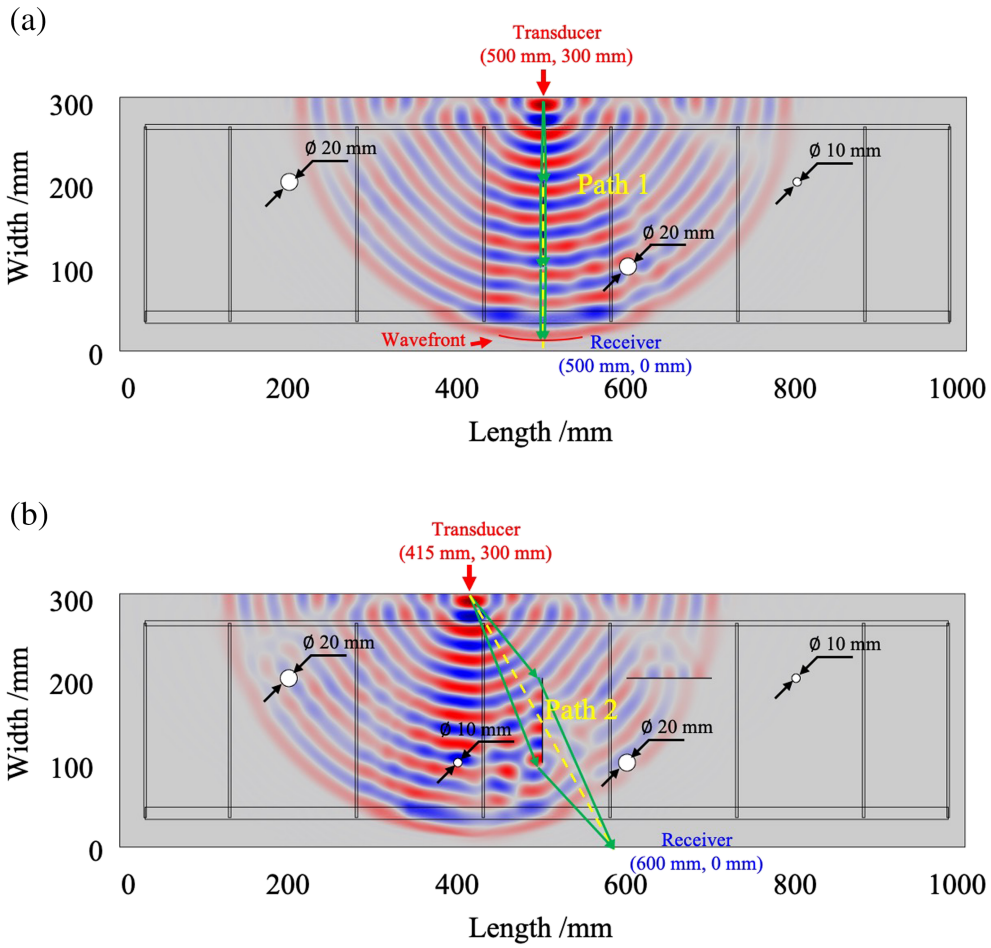

FIGURE 12 (a) Wave propagation example when the transducer locates at (500 mm, 300 mm) and the receiver at (500 mm, 0 mm), and (b) wave propagation example when the transducer locates at (415 mm, 300 mm) and the receiver at (600 mm, 0 mm)

capture the waveform from the bottom side with a sampling frequency of 25 MHz (time resolution 0.04 μs). The velocities of the concrete and steel are mentioned previous, and the wavelength of the ultrasonic wave is 0.08 m. The ToF of the ultrasonic wave in the specimen can be obtained according to the time difference between the emitting and receiving. The NU 62 ultrasonic testing instrument and the input signal are shown in Figure 16.

The size of pixel is chosen as 2.5 cm × 1 cm to reconstruct the internal situation of the RC specimen. Considering the edge of the specimen is not easy to be attached for the piezoelectric probes, the interrogate area is selected to be 800 mm × 300 mm. The number of total pixels is $w = 33 \times 30 = 990$. For the traditional UCT reconstruction, there are $N = 33 \times 33 = 1{,}089$ measurements path in the original dense net, while, for the CS-based UCT approach, 200 measurement paths ($m = 200 > \mu K \log(N/K) = 141$) is enough to localize and reconstruct the damage in the RC specimen. A measurement matrix $\mathbf{\Phi}$ is processed based on Bernoulli distribution to randomly select the measurement paths from the original measurement net. For each measurement path, the excitation is applied 5 times with waveforms averaged to remove measurement noise to derive precise ToF. The ToF measured by the ultrasonic wave are subtracted by the calculated reference and assembled to the ToF difference vector according to the measurement matrix $\mathbf{\Phi}$. The selected paths are sequentially measured via the movement of the actuating and sensing probes. The measurement paths selected from the original net are shown in Figure 17.

As shown in Figure 18, the ToFs of ultrasonic waves carry the information of different internal damaged situations along the four straight-line measurement paths: 70.72 μs for Path A without any damage, 71.64 μs for Path B with a hole, 71.16 μs for Path C parallel to a crack, and 74.24 μs for Path D perpendicular to the crack. The ToFs of the ultrasonic waves are obtained by the first arriving peak indicated by a short green bar and shown in Figure 18b.

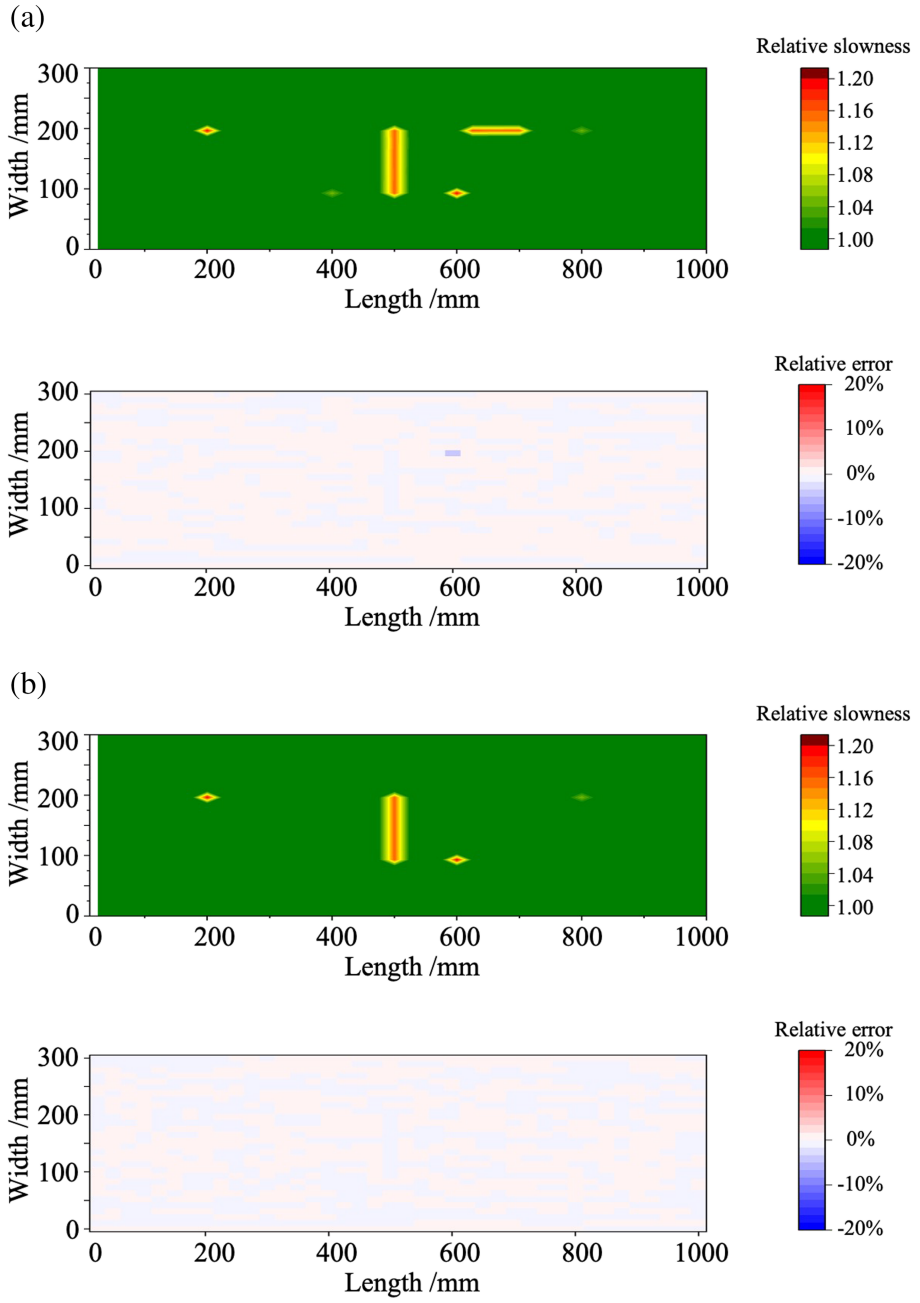

FIGURE 13 Reconstructed results and relative error for Case 3: (a) $z = 50$ mm plane, and (b) $z = 150$ mm plane

For the reconstruction and imaging stage, after assembling the transfer matrix ($\boldsymbol{\Theta} = \boldsymbol{\Phi}\mathbf{A}$) and ToF difference vector ($\Delta\mathbf{T}$), the slowness is calculated by $\ell 1$-minimization method in the CS framework. The threshold $\Delta\overline{\mathbf{S}}_0$ is set to be 0.0008, which means the damage size less than 0.1 mm will be ignored. Meanwhile, the measurements also show the effect caused by steel bar is rather small and negligible compared to concrete because of the small diameter and like-concrete propagating velocity of steel bars. The identification of slowness and damage location is shown in Figure 19. The location and size of hole damages are identified as (200 mm, 100 mm, 9.64 mm), (300 mm, 200 mm, 14.25 mm), (400 mm, 100 mm, 18.87 mm), and (650 mm, 100 mm, 19.66 mm), respectively. The maximum error of the identified result of hole-like damage is 5.6%. Three cracks have also been reconstructed: Most identified results of the vertical crack are in the range of 2.86–3.34 mm, the maximum of the identified result is 4.12, and maximum error is 1.12 mm; the identified results of the horizontal crack are in the range of 3.52–4.89 mm, the maximum error is 1.89 mm; the identified results of the 45° crack are from 2.94–3.35 mm, the maximum error is 0.35 mm. The reconstructed results have

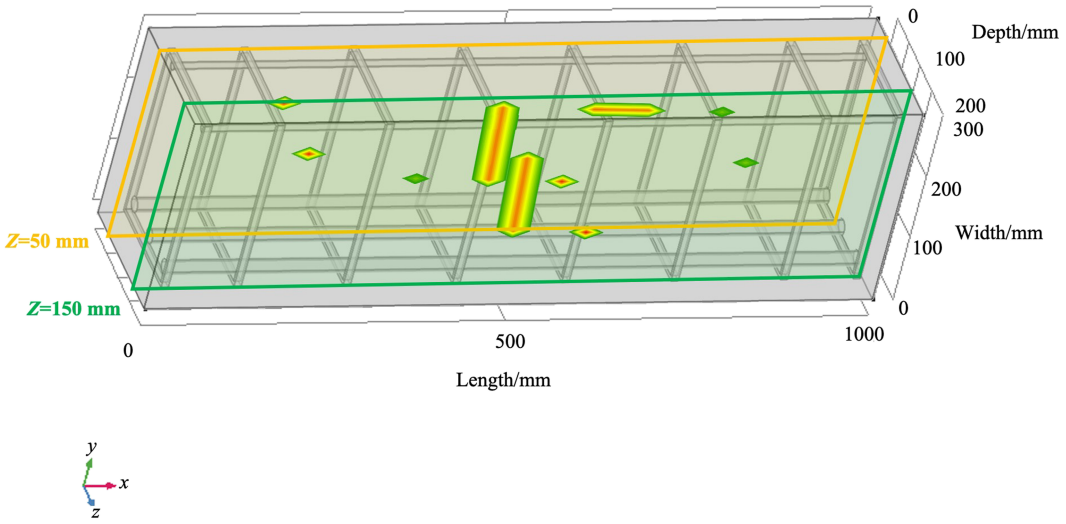

FIGURE 14 Assembled 3-D monitoring results by proposed CS-based UCT inspection

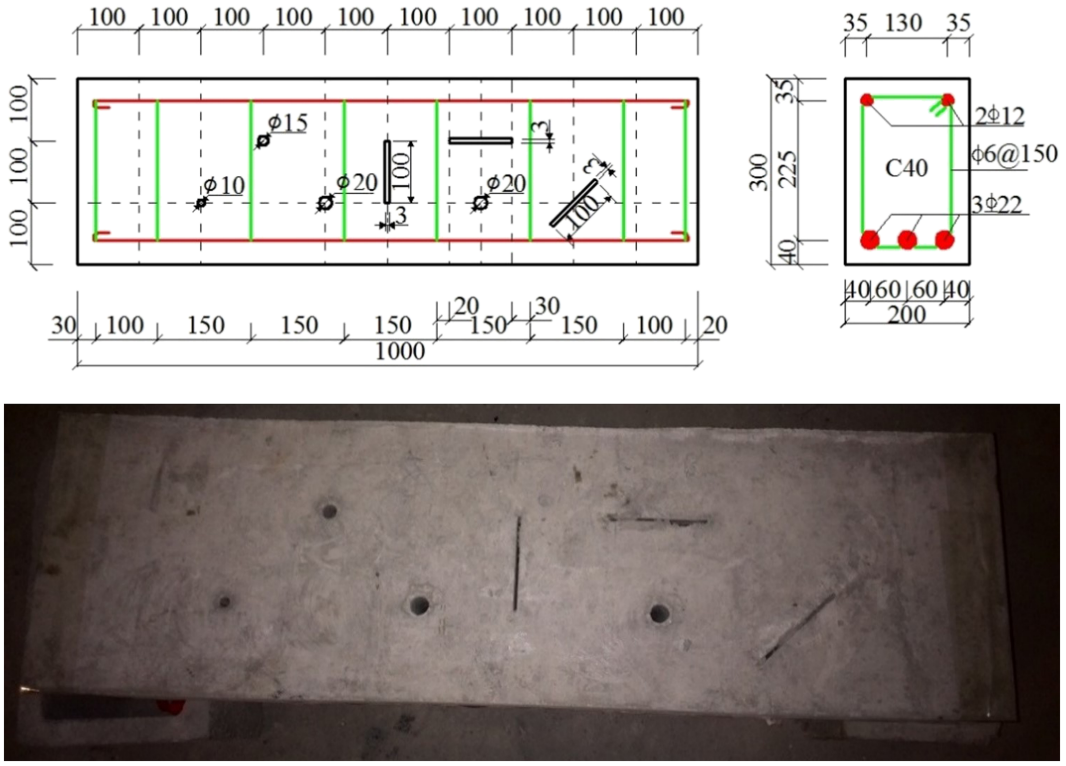

FIGURE 15 Designed and damage distribution in the RC specimen for laboratory experiment

good agreements with the original damages set in the RC specimen, which demonstrate the proposed approach has great potential of cost-efficient identifying damage in the structure via much less measurements.

5 | CONCLUSION

In this paper, based on the naturally sparse distribution of damages, CS theory is proposed as a tool to improve the traditional UCT technique for damage localization in the structures. This sensing strategy is conducted via significantly reducing the number of measurement paths in the measurement stage and reconstructing the slowness values of each

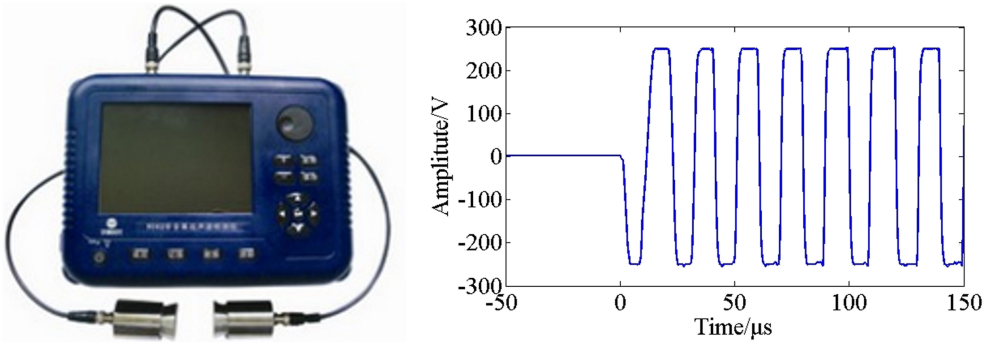

FIGURE 16 Ultrasonic pitch-catch instrument and the excitation signal

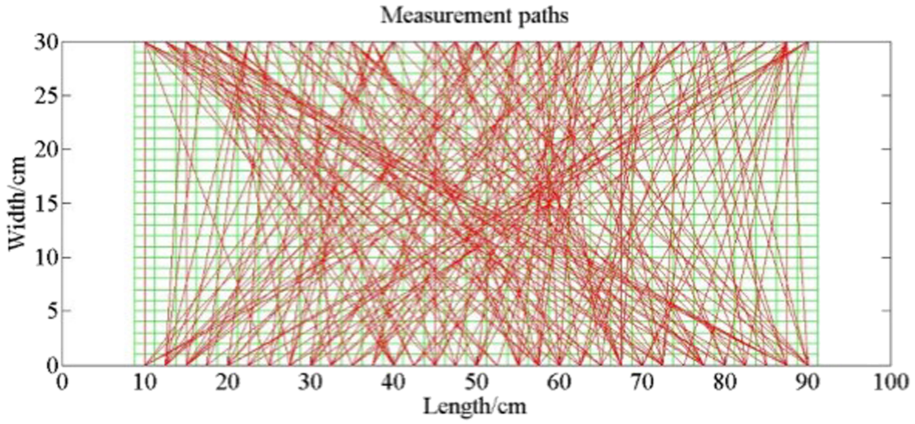

FIGURE 17 Randomly selected measurement paths in the experiment

pixel using $\ell 1$-minimization optimization algorithm in the imaging stage. Ultrasonic waves are introduced into the structural specimen to interrogate the structure by random selected measurement paths to assemble the ToFs vector for reconstruction. The functionality of the CS-based UCT technique is validated on RC models with various damages of both numerical simulation and experimental study in the laboratory.

An important contribution of this study is to invent a novel baseline-free β index to quantitatively assess the performance of the random-selected measurement net. The β index advances our understanding of the redundancy level and balanced distribution of the measurement net in real-world applications. A higher β-index value represents a sparser and better assigned measurement paths for the CS-based UCT technique.

The proposed cost-efficient approach developed both inspection and reconstruction. Considering the damages distribute sparsely in the structure, the proposed approach requires much fewer paths (12.5%–18.3% of the original number), and each measurement path of ultrasonic wave is randomly selected according to a measurement matrix. Then, the slowness of each refined pixel is pursued by solving the $\ell 1$-minimization method in the CS framework. The reconstructed results have good agreements with the preset damages, which reveal the proposed approach is a promising method provides more efficient approach for localizing and imaging the damage with much fewer measurements. CS-based UCT technique is a game-changing approach requiring 20% or less workload compared to the traditional UCT inspection. It has the immense potential in both academic development and industrial applications for SHM.

It is noted that, we demonstrate the capability of damage detection in RC in this paper, this proposed method has great potential in spatial damage detection in concrete, metal, and composite structures as well. The identification error depends on the pixel size and the SNR. Future work will also explore the proposed method to classify more damage types in various structures. Meanwhile, choosing measurement paths from the original net for interrogation will be explored as an optimization problem of the proposed CS-based UCT technique.

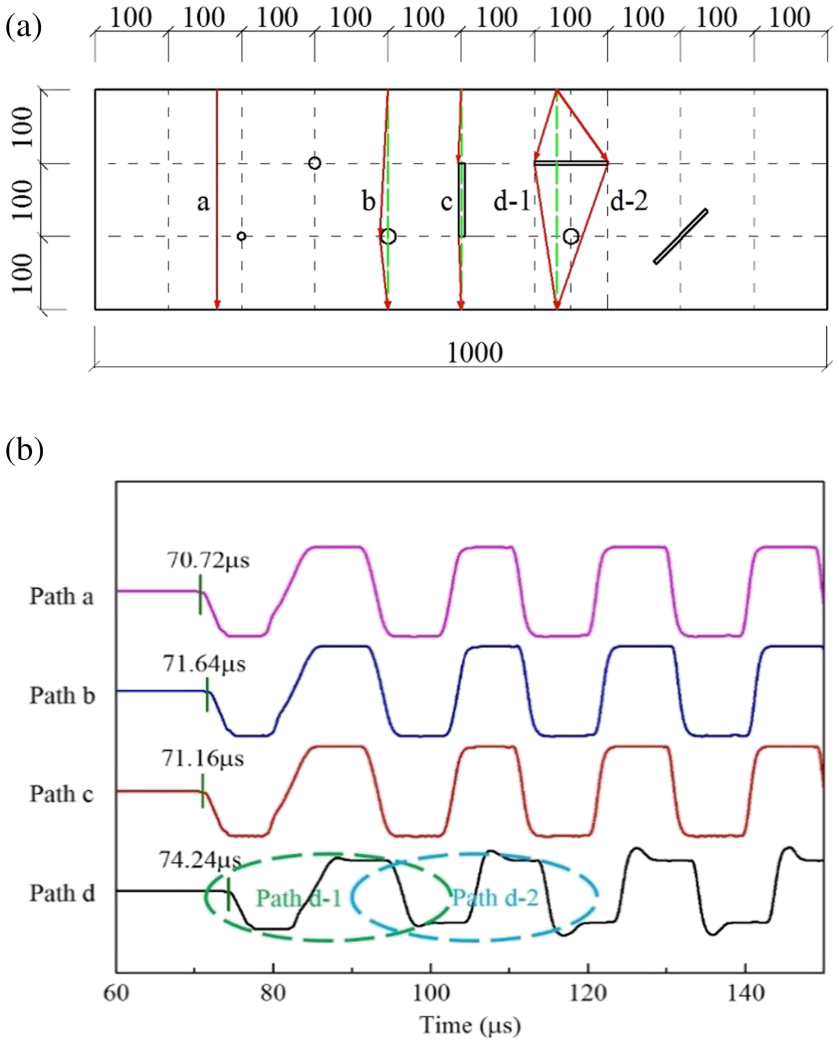

FIGURE 18 (a) Ultrasonic wave propagation paths with different damages, and (b) received waveforms of the ultrasonic waves via the measurement paths above

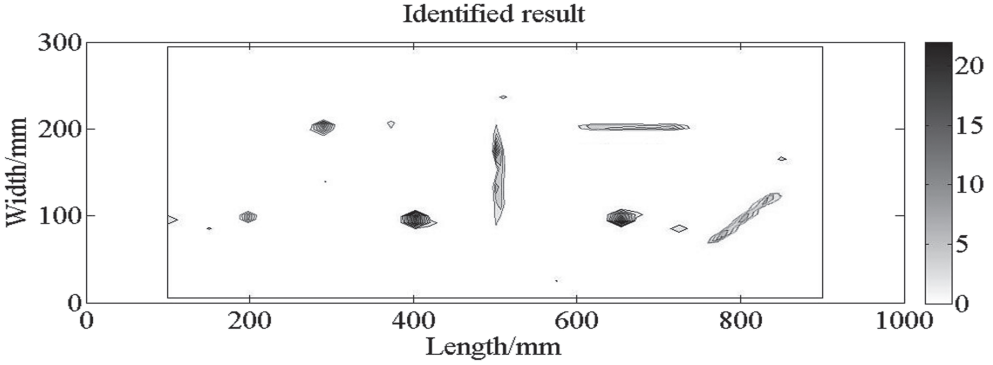

FIGURE 19 Reconstructed results based on the proposed approach

ACKNOWLEDGMENT

The authors express their sincere appreciation to Prof. Hongwei Deng of Harbin Institute of Technology for his great help in the test.

FUNDING INFORMATION

This study is financially supported by the project supported by Natural Science Foundation of China with grant No. 51378154, and major project supported by the China Railway Corporation (CRC) with grant No. 2013G004-A-1.

AUTHOR CONTRIBUTIONS

Wentao Wang was responsible for the methodology, experiment, writing - original draft, and revising the manuscript. Hui Li was responsible for the supervision and revising the manuscript. Chonghe Wang was responsible for the experiment, data collection, and writing - original draft. Wensong Zhou was responsible for the methodology and revising the manuscript. Yuequan Bao was responsible for the methodology and revising the manuscript.

CONFLICT OF INTERESTS

The author declares that there is no conflict of interest.

ORCID

Wentao Wang https://orcid.org/0000-0003-1811-1748
Hui Li https://orcid.org/0000-0001-9198-3951
Wensong Zhou https://orcid.org/0000-0003-3461-0862
Yuequan Bao https://orcid.org/0000-0001-7553-366X

REFERENCES

1. Chang PC, Flatau A, Liu S. Health monitoring of civil infrastructure. *Struct Health Monit*. 2003;2(3):257-267.
2. Rytter A. Vibrational based inspection of civil engineering structures. Dept. of Building Technology and Structural Engineering, Aalborg University. 1993.
3. Balageas D, Fritzen C-P, Güemes A. *Structural Health Monitoring*. John Wiley & Sons; 2010.
4. An Y, Chatzi E, Sim SH, Laflamme S, Blachowski B, Ou J. Recent progress and future trends on damage identification methods for bridge structures. *Struct Control Health Monit*. 2019;26(10):2416-2445.
5. Sohn H, Farrar CR, Hemez FM, Shunk DD, Stinemates DW, Nadler BR, Czarnecki JJ. A review of structural health monitoring literature: 1996–2001, Los Alamos National Laboratory, USA. 2003.
6. Ghosh D, Beniwal S, Ganguli A, Mukherjee A. Reference free imaging of subsurface cracks in concrete using Rayleigh waves. *Struct Control Health Monit*. 2018;25(10):2246-2261.
7. Zhou C, Zhang C, Su Z, Yue X, Xiang J, Liu G. Health monitoring of rail structures using guided waves and three-dimensional diagnostic imaging. *Struct Control Health Monit*. 2017;24(9):1966-1978.
8. Giurgiutiu V, Zagrai A, J. Jing Bao, Piezoelectric wafer embedded active sensors for aging aircraft structural health monitoring. *Struct Health Monit*. 2002;1(1):41-61.
9. Lynch JP, Loh KJ. A summary review of wireless sensors and sensor networks for structural health monitoring. *Shock Vib Digest*. 2006;38(2):91-130.
10. Su Z, Ye L, Lu Y. Guided Lamb waves for identification of damage in composite structures: A review. *J Sound Vib*. 2006;295(3-5):753-780.
11. Wang P, Zhou W, Bao Y, Li H. Ice monitoring of a full-scale wind turbine blade using ultrasonic guided waves under varying temperature conditions. *Struct Control Health Monit*. 2018;25(4):2138-2154.
12. Wang W, Zhang H, Lynch JP, Cesnik CE, Li H. Experimental and numerical validation of guided wave phased arrays integrated within standard data acquisition systems for structural health monitoring. *Struct Control Health Monit*. 2018;25(6):2171-2187.
13. Kak AC. Computerized tomography with X-ray, emission, and ultrasound sources. *Proc IEEE*. 1979;67(9):1245-1272.
14. Tomikawa Y, Iwase Y, Arita K, Yamada H. Nondestructive inspection of a wooden pole using ultrasonic computed tomography. *IEEE T Ultrason*. 1986;33(4):354-358.
15. Yang Y, Dorn C, Mancini T, et al. Reference-free detection of minute, non-visible, damage using full-field, high-resolution mode shapes output-only identified from digital videos of structures. *Struct Health Monit*. 2018;17(3):514-531.
16. Park J-W, Lee J-J, Jung H-J, Myung H. Vision-based displacement measurement method for high-rise building structures using partitioning approach. *Ndt & E Int*. 2010;43(7):642-647.
17. Greenleaf J, Ylitalo J, Gisvold JJ. Ultrasonic computed tomography for breast examination. *IEEE Eng Med Biol Mag*. 1987;6(4):27-32.
18. Tegos TJ, Sabetai MM, Nicolaides AN, Elatrozy TS, Dhanjil S, Stevens JM. Patterns of brain computed tomography infarction and carotid plaque echogenicity. *J Vasc Surg*. 2001;33(2):334-339.

19. Wang LV. Multiscale photoacoustic microscopy and computed tomography. *Nature Photonics*. 2009;3(9):503-509.
20. Snow J Jr, Goldstein H, Wallace S. Comparison of scintigraphy, sonography, and computed tomography in the evaluation of hepatic neoplasms. *Am J Roentgenol*. 1979;132(6):915-918.
21. Greenleaf JF, Bahn RC. Clinical imaging with transmissive ultrasonic computerized tomography. *IEEE Trans Biomed Eng*. 1981;28(2):177-185.
22. Bond LJ, Kepler WF, Frangopol DM. Improved assessment of mass concrete dams using acoustic travel time tomography. Part I—theory. *Construct Build Mater*. 2000;14(3):133-146.
23. Kepler WF, Bond LJ, Frangopol DM. Improved assessment of mass concrete dams using acoustic travel time tomography. Part II—application. *Construct Build Mater*. 2000;14(3):147-156.
24. Ohkawa M, Kawata N, Uchida S. Cross-sectional distributions of gas and solid holdups in slurry bubble column investigated by ultrasonic computed tomography. *Chem Eng Sci*. 1999;54(21):4711-4728.
25. Fujii M, Zhang X. Noncontact measurement of internal temperature distribution in a solid material using ultrasonic computed tomography. *Exp Therm Fluid Science*. 2001;24(3-4):107-116.
26. Wiegand F, Hoyle BS. Simulations for parallel processing of ultrasound reflection-mode tomography with applications to two-phase flow measurement. *IEEE T Ultrason*. 1989;36(6):652-660.
27. Xu LJ, Han YT, Xu LA, Yang JS. Application of ultrasonic tomography to monitoring gas/liquid flow. *Chem Eng Sci*. 1997;52(13):2171-2183.
28. Zhu N, Jiang Y, Kato S. Ultrasonic computerized tomography (CT) for temperature measurements with limited projection data based on extrapolated filtered back projection (FBP) method. *Energy*. 2005;30(2-4):509-522.
29. Hay T, Royer R, Gao HD, Zhao X, Rose J. A comparison of embedded sensor Lamb wave ultrasonic tomography approaches for material loss detection. *Smart Mater Struct*. 2006;15(4):946-951.
30. Hoyle B. Process tomography using ultrasonic sensors. *Meas Sci Technol*. 1996;7(3):272-280.
31. Rahiman M, Rahim RA, Zakaria Z. Design and modelling of ultrasonic tomography for two-component high-acoustic impedance mixture. *Sensors Actuators A: Phys*. 2008;147(2):409-414.
32. Filipík A, Jan J, Peterlík I. Time-of-flight based calibration of an ultrasonic computed tomography system. *Radio Engineering*. 2012;21:533-544.
33. Martin J, Broughton K, Giannopolous A, Hardy M, Forde M. Ultrasonic tomography of grouted duct post-tensioned reinforced concrete bridge beams. *NDT & E Int*. 2001;34(2):107-113.
34. Candès EJ, Wakin MB. An introduction to compressive sampling. *IEEE Signal Proces Magazine*. 2008;25(2):21-30.
35. Candès EJ. Compressive sampling. *Proc Int Congress Maths*. 2006;1433-1452.
36. Donoho DL. Compressed sensing. *IEEE Trans Inf Theory*. 2006;52(4):1289-1306.
37. Candès EJ, Romberg J, Tao T. Robust uncertainty principles: Exact signal reconstruction from highly incomplete frequency information. *IEEE Trans Inf Theory*. 2006;52(2):489-509.
38. Candes EJ, Romberg JK, Tao T. Stable signal recovery from incomplete and inaccurate measurements. *Commun Pure Appl Math*. 2006;59(8):1207-1223.
39. Baraniuk RG. More is less: signal processing and the data deluge. *Science*. 2011;331(6018):717-719.
40. Baraniuk RG. Compressive sensing. *IEEE Signal Proc Mag*. 2007;24(4):118-121.
41. Davenport MA, Boufounos PT, Wakin MB, Baraniuk RG. Signal processing with compressive measurements. *IEEE J Selected Topics Signal Proces*. 2010;4(2):445-460.
42. Lustig M, Donoho D, Pauly JM. Sparse MRI: The application of compressed sensing for rapid MR imaging. *Magn Reson Med*. 2007;58(6):1182-1195.
43. Lustig M, Santos JM, Donoho DL, Pauly JM. kt SPARSE: High frame rate dynamic MRI exploiting spatio-temporal sparsity, Proceedings of the 13th Annual Meeting of ISMRM, Seattle, Washington, USA, 2006.
44. Yao HJ, Gerstoft P, Shearer PM, Mecklenbrauker C. Compressive sensing of the Tohoku-Oki Mw 9.0 earthquake: frequency-dependent rupture modes. *Geophys Res Lett*. 2011;38(20):61-65.
45. Lin TT, Herrmann FJ. Compressed wavefield extrapolation. *Geophysics*. 2007;72(5):77–93.
46. Bao YQ, Beck JL, Li H. Compressive sampling for accelerometer signals in structural health monitoring. *Struct Health Monit*. 2011;10:235-246.
47. Malioutov D, Cetin M, Willsky AS. A sparse signal reconstruction perspective for source localization with sensor arrays. *IEEE Trans Signal Proc*. 2005;53(8):3010-3022.
48. Foucart S, Rauhut H. A mathematical introduction to compressive sensing. In: *A Mathematical Introduction to Compressive Sensing*. Springer; 2013:1-39.
49. Chang M, Yuan S, Guo F. Corrosion monitoring using a new compressed sensing-based tomographic method. *Ultrasonics*. 2020;101:105988-105998.
50. Mokhtari AA, Ohadi A, Amindavar H. Polygonal damage shape reconstruction in plates using guided Lamb wave. *Struct Control Health Monit*. 2017;24(5):1907-1925.
51. Jansen D, Hutchins D. Immersion tomography using Rayleigh and Lamb waves. *Ultrasonics*. 1992;30(4):245-254.
52. Malyarenko EV, Hinders MK. Ultrasonic Lamb wave diffraction tomography. *Ultrasonics*. 2001;39(4):269-281.

53. Wang W, Lynch JP. IWSHM 2017: Application of guided wave methods to quantitatively assess healing in osseointegrated prostheses. *Struct Health Monit*. 2018;17(6):1377-1392.
54. Hoskins PR. Principles of ultrasound elastography. *Ultrasound*. 2012;20(1):8-15.
55. Born M, Wolf E. Principles of optics: electromagnetic theory of propagation, interference and diffraction of light. *CUP Archive*. 2000; 53(10):77-78.
56. Banerjee S, Leckey CA. *Computational Nondestructive Evaluation Handbook: Ultrasound Modeling Techniques*. CRC Press; 2020.
57. Müller G, Möser M. *Handbook of Engineering Acoustics*. Springer Science & Business Media; 2012.
58. Kapralos B, Jenkin M, Milios E. Acoustical diffraction modeling utilizing the Huygens-Fresnel principle, IEEE International Workshop on Haptic Audio Visual Environments and their Applications. 2005.

How to cite this article: Wang W, Li H, Wang C, Zhou W, Bao Y. An improved ultrasonic computerized tomography (UCT) technique for damage localization based on compressive sampling (CS) theory. *Struct Control Health Monit*. 2022;29(6):e2938. doi:10.1002/stc.2938

APPENDIX A

In generally, the velocity of the ultrasonic wave in concrete is 3,800–4,500 m/s, and the velocity of ultrasonic wave propagating in steel and air are about 5,200s and 340 m/s,[54] respectively. Considering the acoustic impedance of the materials above, the acoustic impedance of air is much less than the acoustic impedance of concrete and steel. Thus, ultrasonic wave will reflect and propagate back when it reaches the concrete-air boundary. The ratio of reflected pressure to incident ultrasonic pressure is called reflection coefficient (indicated by the symbol R),[55] which is determined by the acoustic impedance of concrete and air, as shown in Equation (A1):

$$R = \frac{p_r}{p_0} = \frac{z_2 - z_1}{z_2 + z_1}, \tag{A1}$$

where, z_2 is the acoustic impedance of concrete, z_1 is the acoustic impedance of air (almost equal to 0), p_r is the reflected ultrasonic pressure, and p_0 is the incident ultrasonic pressure.

In fact, the impedance of concrete $z_2 \approx 108 \times 10^4 g/cm^2$, and the impedance of air $z_1 \approx 0.004 \times 10^4 \mathrm{g/cm}^2$.[57] Considering the relationship of dense medium (concrete) and the sparse medium (air), the energy transmits to air is so little that we can ignore it ($z_1 \ll z_2$, $R \approx 1$, $p_t \ll p_r$). The majority of energy remains in the concrete (shown in Figure A1).

The acoustic impedances for concrete and steel are very close; thus, the ultrasonic waves can propagate from concrete into the steel bar, vice versa. While damage parts in structures (e.g., holes or cracks) are filled by air and should be regarded as an obstacle for the ultrasonic wave in structures. Based on Huygens–Fresnel principle, every point on the previous wavefront is a source of next spherical waves, and the new wavefront is a line tangent to all the spherical waves.[56–58] When the ultrasonic wave encounters an obstacle, only points that are not obscured by the obstacle remains. Thus, the new wavefront is distorted by the obstacle, which results in the ultrasonic wave bypassing the damage via its edges with longer travel length and larger ToF, as shown in Figure A2. The wavefront propagation is similar when multiple damages get involved in the ultrasonic propagation.

Cracks are directional damages in structures, as shown in Figure A3, the difference ToF measured along measurement Path 1 (ΔT_1) dramatically differs from that obtained along Path 2 (ΔT_2). Thus, the direction of crack can be predicted by the relationships of difference ToFs ($\Delta \mathbf{T}$) and the measurement paths.

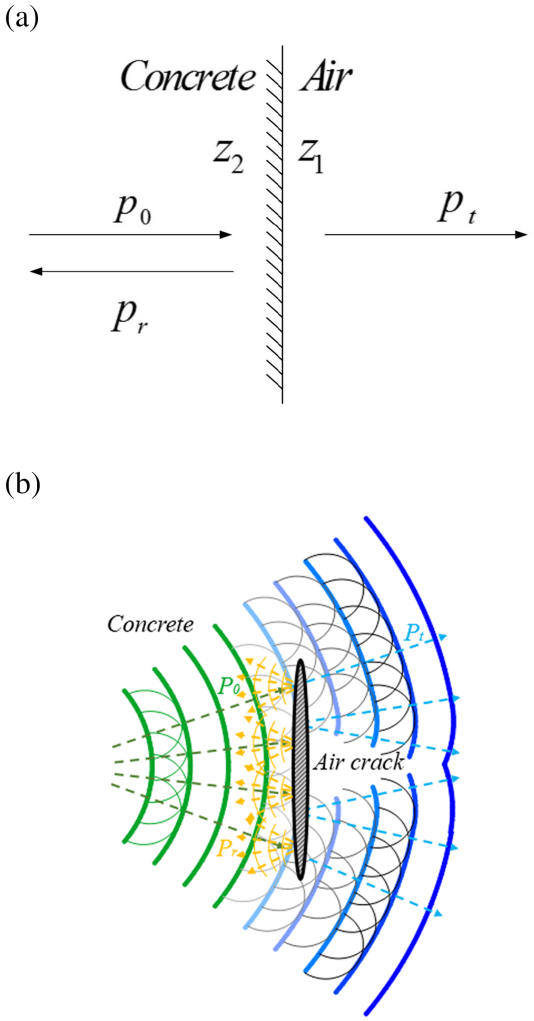

FIGURE A1 Schematic of concrete-air interface reflection: (a) reflection and acoustic impedance, (b) wavefront based on Huygens–Fresnel principle

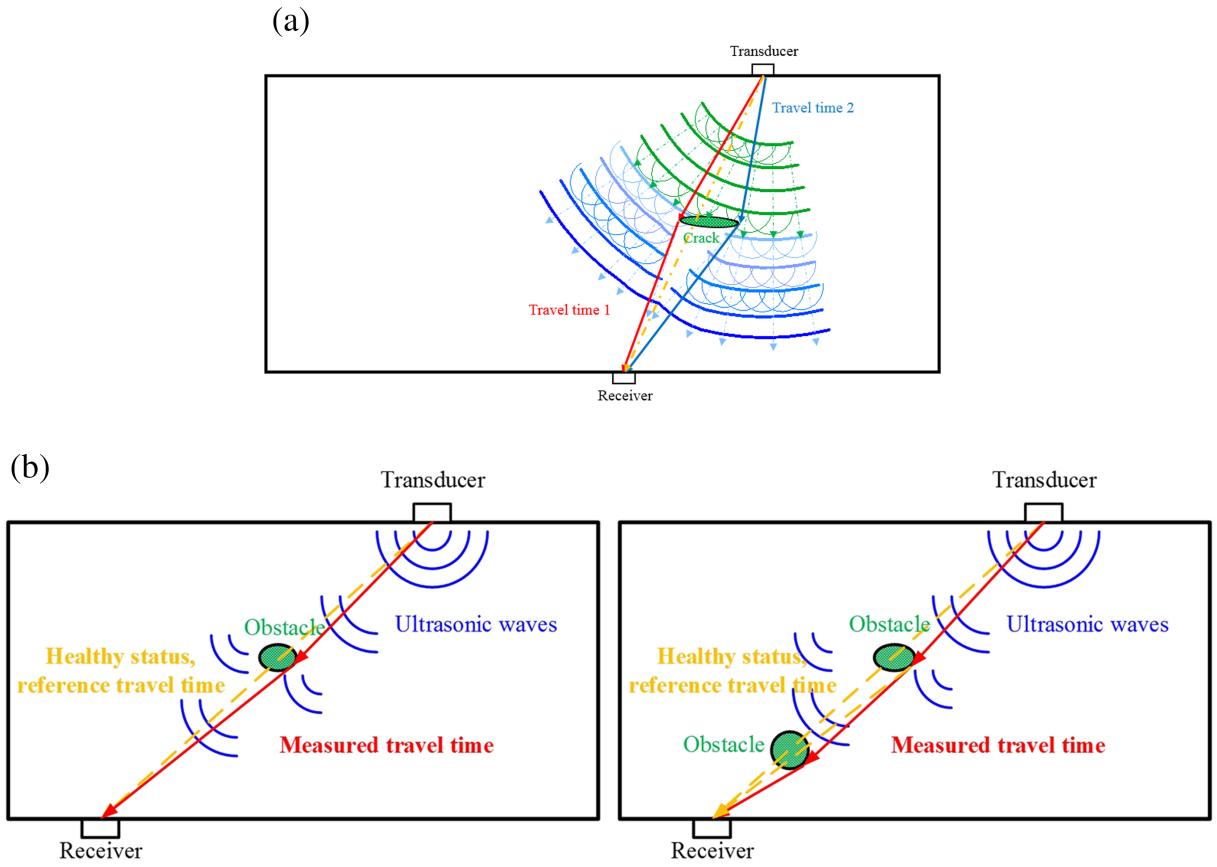

FIGURE A2 Propagation properties of ultrasonic waves in damaged structures: (a) shortest propagation path from the transducer to receiver, (b) comparison of one damage and multiple damages in the structures

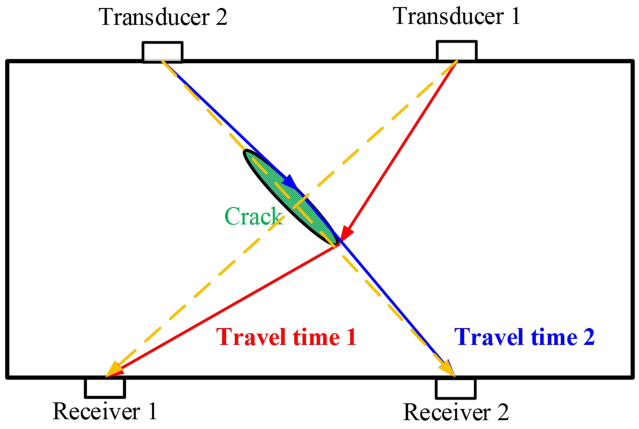

FIGURE A3 Directional characteristic of crack measured by different paths